

Effect of PVP Molecular Weights on the Synthesis of Ultrasmall CuS Nanoflakes: Synthesis, Properties, and Potential Application for Phototheranostics

Madhavi Tripathi, Ananya Sharma, Sanhita Sinharay,* and Ashok M. Raichur*



Cite This: *ACS Appl. Bio Mater.* 2024, 7, 1671–1681



Read Online

ACCESS |



Metrics & More



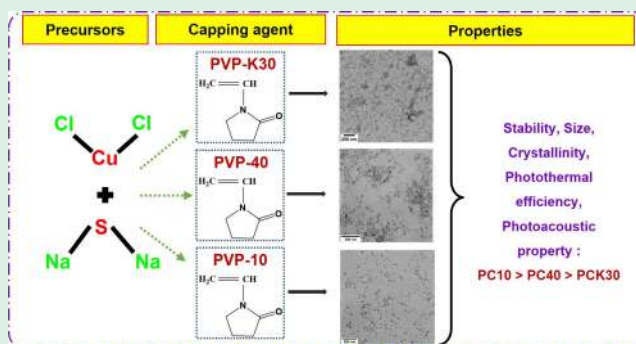
Article Recommendations



Supporting Information

ABSTRACT: Copper sulfide nanoparticles (CuS) hold tremendous potential for applications in photothermal therapy (PTT) and photoacoustic imaging (PAI). However, the conventional chemical coprecipitation method often leads to particle agglomeration issues. To overcome this challenge, we utilized polyvinylpyrrolidone (PVP) as a stabilizing agent, resulting in the synthesis of small PVP-CuS nanoparticles named PC10, PCK30, and PC40. Our study aimed to investigate how different molecular weights of PVP influence the nanoparticles' crystalline characteristics and essential properties, especially their photoacoustic and photothermal responses. While prior research on PVP-assisted CuS nanoparticles has been conducted, our study delves deeper into this area, providing insights into optical properties. Remarkably, all synthesized nanoparticles exhibited a crystalline structure, were smaller than 10 nm, and featured an absorbance peak at 1020 nm, indicating their robust photoacoustic and photothermal capabilities. Among these nanoparticles, PC10 emerged as the standout performer, displaying superior photoacoustic properties. Our photothermal experiments demonstrated significant temperature increases in all cases, with PC10 achieving an impressive efficiency of 51%. Moreover, cytotoxicity assays revealed the nanoparticles' compatibility with cells, coupled with an enhanced incidence of apoptosis compared to necrosis. These findings underscore the promising potential of PVP-stabilized CuS nanoparticles for advanced cancer theranostics.

KEYWORDS: photoacoustics, photothermal therapy, copper sulfide, theranostics, nanoparticles



1. INTRODUCTION

The effective initiation of cancer treatment necessitates the utilization of cancer diagnostic imaging techniques to gain a comprehensive understanding of the tumor environment, encompassing its cellular features and heterogeneities. These innovative systems amalgamate various diagnostic modalities such as CT, MRI, ultrasound, and PET, together with therapeutic strategies, thereby enhancing treatment outcomes for a broad spectrum of diseases, including cancer.^{1–3} Nanoparticles have emerged as promising agents in the development of such integrated systems capable of performing both diagnosis and therapy simultaneously. This approach enables the detection of early stage cancers, facilitates the monitoring of therapeutic outcomes, and opens up avenues for precision medicine.^{4–6} Among the rapidly advancing optical imaging technologies, photoacoustic imaging (PAI) has garnered significant attention. PAI utilizes laser pulses to excite target molecules and tissues, inducing localized thermal expansion that generates detectable acoustic signals, thereby unraveling the distinctive properties of the target site.^{7,8} PAI employs both exogenous and endogenous contrast agents to create detailed images of the tissues. However, the utilization

of efficient exogenous contrast agents assumes critical importance for achieving enhanced specificity and sensitivity, as endogenous contrast agents have limited utility in revealing the pathophysiological state of diseases.⁹ Notably, a majority of nanoparticle-based PAI contrast agents exhibit remarkable photothermal efficiency by converting light into heat, thus generating hyperthermia that can be employed for photothermal therapy (PTT).^{10,11} It is intriguing to note that both PAI and PTT operate based on the principles of photothermal conversion, thus enabling their combined utilization for diagnosis and therapy purposes.^{10,11}

Nanoparticles demonstrate exceptional versatility, owing to their adjustable properties, and have found value in a wide range of biomedical applications such as sensors, molecular

Received: November 24, 2023

Revised: February 21, 2024

Accepted: February 22, 2024

Published: March 6, 2024



probes, contrast agents, optical biosensors, and therapeutic and theranostic platforms.^{12–15} Important considerations for these applications include the biocompatibility, water dispersibility, appropriate size, and biofunctionalization of nanoparticles.^{16,17} The effectiveness of nanoparticles arises from their ability to adapt to the aqueous nature of biological environments and their efficient interactions with diverse biochemical groups, enabling access to various biological settings.^{17,18} Additionally, the size of nanoparticles plays a significant role in determining their physical and chemical properties, colloidal behavior, size-dependent interactions, and their accessibility to different tissue environments.^{12,19}

Copper-based chalcogenides emerge as a promising class of nanoparticles for a broad range of biomedical applications including biosensors, electrochemical sensors, photocatalysts, drug delivery agents, and contrast probes.^{20–22} Among these, copper sulfide nanoparticles have gained considerable attention due to their tunable optical and electrochemical properties.²³ Copper sulfide nanoparticles can exist in various stoichiometries, ranging from copper-rich chalcocite (Cu_2S) to copper-deficient covellite (CuS), with the optical bandgap energy varying from 1.2 to 2.5 eV depending on the stoichiometry.²⁴ Moreover, copper sulfide nanoparticles exhibit diverse physical and chemical properties, dictated by their sizes and shapes. Notably, the CuS phase is of particular interest, as it demonstrates a high free carrier density, leading to localized surface plasmon resonance (LSPR). The oscillation of excess free carriers results in absorbance in the near-infrared (NIR) range, making copper sulfide nanoparticles well-suited for applications in photothermal therapy (PTT) and photoacoustic imaging (PAI).^{25,26}

An array of synthesis methods has been employed to create copper sulfide nanoparticles with diverse sizes and morphologies, including solvothermal, hydrothermal, sonochemical, hot injection, and one-step coprecipitation techniques.^{27–29} Among these methods, the chemical coprecipitation approach stands out due to its simplicity, cost-effectiveness, low temperature requirements, and the capability to precisely control particle size and stoichiometry.³⁰ However, a notable challenge associated with the coprecipitation method lies in the tendency for agglomeration during synthesis, which can be effectively addressed through meticulous selection of suitable stabilizing and capping agents.³¹

To obtain small copper sulfide nanoparticles, diverse capping agents and stabilizers, such as bovine serum albumin (BSA), citrate, Pillararene, and polyethylene glycol (PEG), have found application.^{32–35} Among these choices, polyvinylpyrrolidone (PVP), a commonly used nontoxic polymer, offers distinct advantages.³⁶ PVP incorporates functional groups such as $\text{C}=\text{O}$, $\text{C}=\text{N}$, and CH_2 , imparting hydrophilic and hydrophobic components to its structure. Notably, PVP possesses carbonyl oxygens that readily form bonds with water molecules and other solvents. Furthermore, PVP serves as an excellent stabilizer and dispersant, employing repulsive forces generated by its hydrophobic carbon to effectively control nanoparticle aggregation through steric hindrance. Recent simulation studies have provided valuable insights into the correlation between the length of the polymer chain and the shape and size of nanoparticles. Additionally, the concentration of PVP has been demonstrated to influence particle morphology and dimensions.³⁷ However, the impact of different molecular weights of PVP on the synthesis of ultrasmall copper sulfide nanoparticles remains relatively

underexplored.^{38–40} Furthermore, the influence of varying molecular weights of PVP, acting as a capping agent, on the characteristic properties of particles concerning photoacoustic imaging and photothermal responses warrants further investigation.

To delve into the influence of distinct molecular weights of PVP on the structural and optical properties of CuS nanoparticles, we employed a one-pot synthesis approach. By employing varying molecular weights of PVP, we synthesized three distinct types of nanoflakes: PC10, PC40, and PCK30. Our investigation focuses on identifying the optimal molecular weight of PVP for synthesizing small CuS nanoflakes, with potential applications in photoacoustic imaging and photothermal therapy.

2. EXPERIMENTAL DETAILS

2.1. Materials. Copper(II) chloride dihydrate ($\text{CuCl}_2 \cdot 2\text{H}_2\text{O}$) was purchased from SRL chemicals. Polyvinylpyrrolidone (PVP-40:40 kDa, PVP-10:10 kDa, PVP-K30:55 kDa) Sodium sulfide (Na_2S), Agar, Dulbecco's Modified Eagle Medium (DMEM) media, 3-[4,5-dimethylthiazol-2-yl]-2,5 diphenyl tetrazolium bromide (MTT), dimethyl sulfoxide (DMSO), phosphate buffer saline (PBS), trypsin, and an apoptosis kit (FITC-labeled Annexin V; propidium iodide (PI)) were purchased from Sigma-Aldrich. Fetal Bovine Serum (FBS) was obtained from GIBCO. All chemicals were used without further purification. Deionized water was used throughout the experiments for the preparation of the dilutions.

2.2. Synthesis. To synthesize PVP-capped CuS nanoflakes, namely PC10, PC40, and PCK30, the coprecipitation method was employed using PVP-10, PVP-40, and PVP-K30, respectively. The synthesis procedure followed an aqueous chemical route through reflux with water used as the solvent. The steps of the synthesis process are illustrated in Figure 1. In summary, 84 mg of PVP was

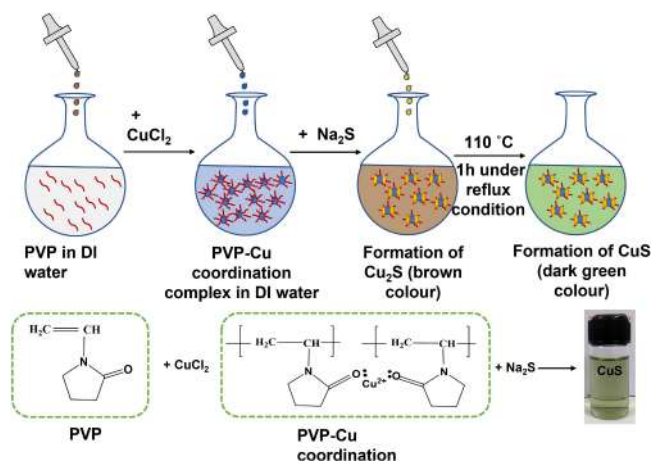


Figure 1. Illustration of coprecipitation process of synthesis. A similar process applies for the synthesis of PC10, PC40, and PCK30.

dissolved in 20 mL of deionized (DI) water and stirred for 30 min until complete dissolution of PVP. The pH of the solution was adjusted to 7. Next, 1 mL of 0.7 M CuCl_2 was added, and the mixture was stirred for an additional 30 min to facilitate interaction between PVP and Cu ions. Na_2S , acting as a sulfur precursor, was gradually added to the solution, leading to a noticeable color change to brown. The molar ratio of S/Cu was maintained at 2.5:1 after optimization. The solution was then refluxed at 110°C for 1 h, resulting in a color transition from brown to dark green, indicating the successful synthesis of CuS nanoflakes. Subsequently, the solution was rapidly cooled to 4°C , and excess reactants were eliminated through dialysis employing a 14 kDa cellulose membrane. Finally, the product was lyophilized.

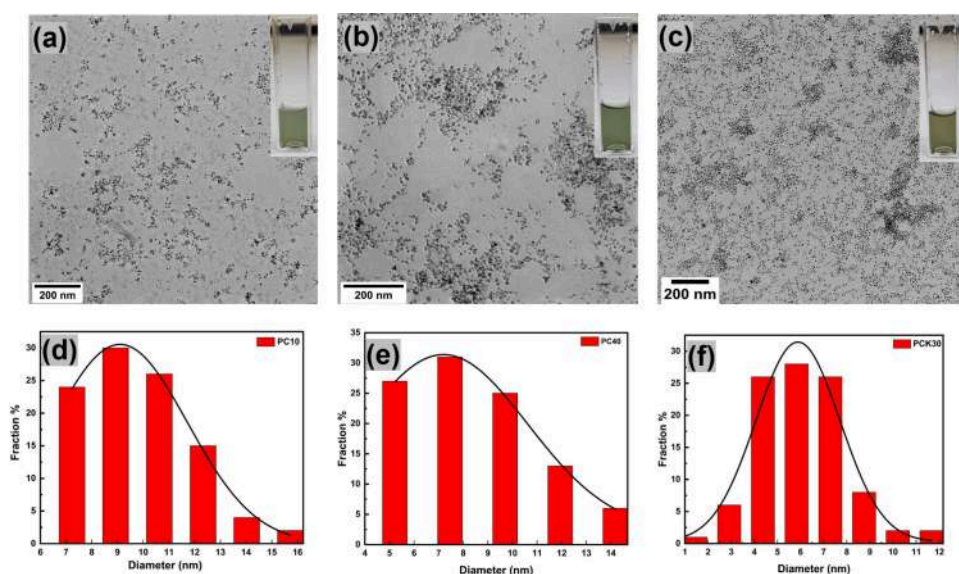


Figure 2. TEM micrograph analysis: (a) TEM image of PC10, (b) TEM image of PC40, and (c) TEM image of PCK30. (d) Particle size distribution of PC10. (e) Particle size distribution of PC40. (f) Particle size distribution of PCK30 (all scale bars 200 nm).

2.3. Characterization. The structural and morphological characterization of the nanoparticles was conducted using a transmission electron microscope (TEM) called Titan Themis 300 kV, formerly known as FEI and currently Thermo. To perform the analysis, a dispersion of the nanoparticles in water was prepared and deposited on a copper grid. After drying, the samples were examined under TEM. For the determination of the oxidation states of the elements within the nanoparticles, X-ray photoelectron spectroscopy (XPS) measurements were performed using a PHI 5000 VersaProbe III instrument from Physical Electronics, USA. To prepare the samples for analysis, a liquid dispersion of the material was drop-casted onto a silicon wafer and subsequently dried in a desiccator. X-ray diffraction (XRD) measurements were carried out on the X'Pert PRO instrument from PANalytical, Netherlands. The analysis was performed by using the powdered form of the nanoparticles. The zeta potential of the nanoparticles was measured by using a Nano ZS instrument from Malvern. UV–visible absorption spectrum analysis was conducted by using a BioTek Synergy Neo2 plate reader. To study the Raman spectra, the LabRAM HR (UV) system, a state-of-the-art RAMAN/PL instrument, was employed.

2.4. Stability. To assess the stability of the synthesized nanoparticles, a 15-day evaluation was carried out at a temperature of 4 °C. The nanoflakes were dispersed in phosphate-buffered saline (PBS), and their surface charge was monitored through zeta potential measurements. It should be noted that the choice of surface coating significantly impacts the physicochemical properties of the nanoflakes. Furthermore, X-ray photoelectron spectroscopy (XPS) studies were conducted to investigate the possibility of nanoparticle oxidation. The binding energy was calibrated with respect to the carbon 1s peak at 284.5 eV, which served as a reference point for the analysis.

2.5. Photothermal Experiments. Various concentrations (10 $\mu\text{g/mL}$, 20 $\mu\text{g/mL}$, 40 $\mu\text{g/mL}$, 60 $\mu\text{g/mL}$, 80 $\mu\text{g/mL}$, 100 $\mu\text{g/mL}$) of PC10, PC40, and PCK30 were prepared in DI water. Adlabs Instruments, 1064 nm, 1 W, continuous wave (CW) laser, was used for all photothermal measurements of the samples. All the temperature monitoring was performed using IR Thermal Camera (Optris GmbH) with an optical resolution of 382×288 pixels. The solutions were irradiated with a 1064 nm Laser of 1 W power to monitor the temperature profile for 5 min. Also, the Photothermal efficiency (η) was calculated using Roper's method.

2.6. Photoacoustic Experiments. To evaluate their suitability as contrast agents for photoacoustic (PA) imaging, PC10, PC40, and PCK30 nanoflakes were incorporated into agar phantoms at different mass concentrations (10, 20, 40, 60, 80, and 100 ppm). Photoacoustic

images of these phantoms were performed on the MSOT inVision instrument (iTHERA Medical, GmbH). The photoacoustic images were processed using the inbuilt inVision software to obtain photoacoustic absorbance (PA) values and a linear correlation between the PA values and phantom concentrations were observed.

2.7. Cytotoxicity Studies. To assess the toxicity of the prepared particles, we performed an MTT assay. A549 (non-small cell lung carcinoma) cells were cultured in 90% Dulbecco's Modified Eagle Medium (DMEM) supplemented with 10% fetal bovine serum (FBS) at 37 °C in a 5% CO₂ humidified environment. Cells were seeded in 96-well plates at a density of 10^4 cells per well, followed by treatment with varying concentrations (10 $\mu\text{g/mL}$, 20 $\mu\text{g/mL}$, 40 $\mu\text{g/mL}$, 60 $\mu\text{g/mL}$, 80 $\mu\text{g/mL}$, 100 $\mu\text{g/mL}$, 120 $\mu\text{g/mL}$, 140 $\mu\text{g/mL}$) of PC10, PC30K, and PC40 for 24 h. Next, MTT was added to the wells and incubated for 4 h before the formazan crystals were dissolved in DMSO, and the absorbance was measured at 560 nm using BioTek Synergy H1 multimode plate reader (please put the model number).

2.8. Apoptosis Studies. To investigate the apoptotic profile of A549 cells treated with 80 $\mu\text{g/mL}$ of various nanoflakes, we utilized FITC-labeled Annexin V (FITC-Annexin V) staining to identify the apoptotic dead cell population. To differentiate necrotic cells from apoptotic ones, cells were simultaneously stained with PI. Following the treatments, cells were collected, washed with PBS, and stained with FITC-Annexin V–PI according to the manufacturer's instructions. The samples were then analyzed using a FACS Verse (BD Biosciences, NJ) flow cytometer, with data collected for 10 000 cells per sample and subsequently analyzed.

3. RESULTS AND DISCUSSION

3.1. Synthesis and Characterizations. In this study, the focus was on synthesizing PVP-capped CuS nanoflakes to investigate the impact of different PVP molecular weights on the properties of CuS. The synthesis process, depicted in Figure 1, commenced with the addition of PVP to water, followed by gentle stirring to facilitate the formation of hydrogen bonds between PVP linear chains and water molecules. Subsequently, the introduction of CuCl₂ into the PVP solution caused dissociation of Cu²⁺ ions. The carbonyl groups present in PVP molecules formed chelation complexes with the Cu ions, resulting in the formation of a blue-colored solution. The subsequent addition of Na₂S led to a change in color from blue to brown, indicating the ionic transfer between

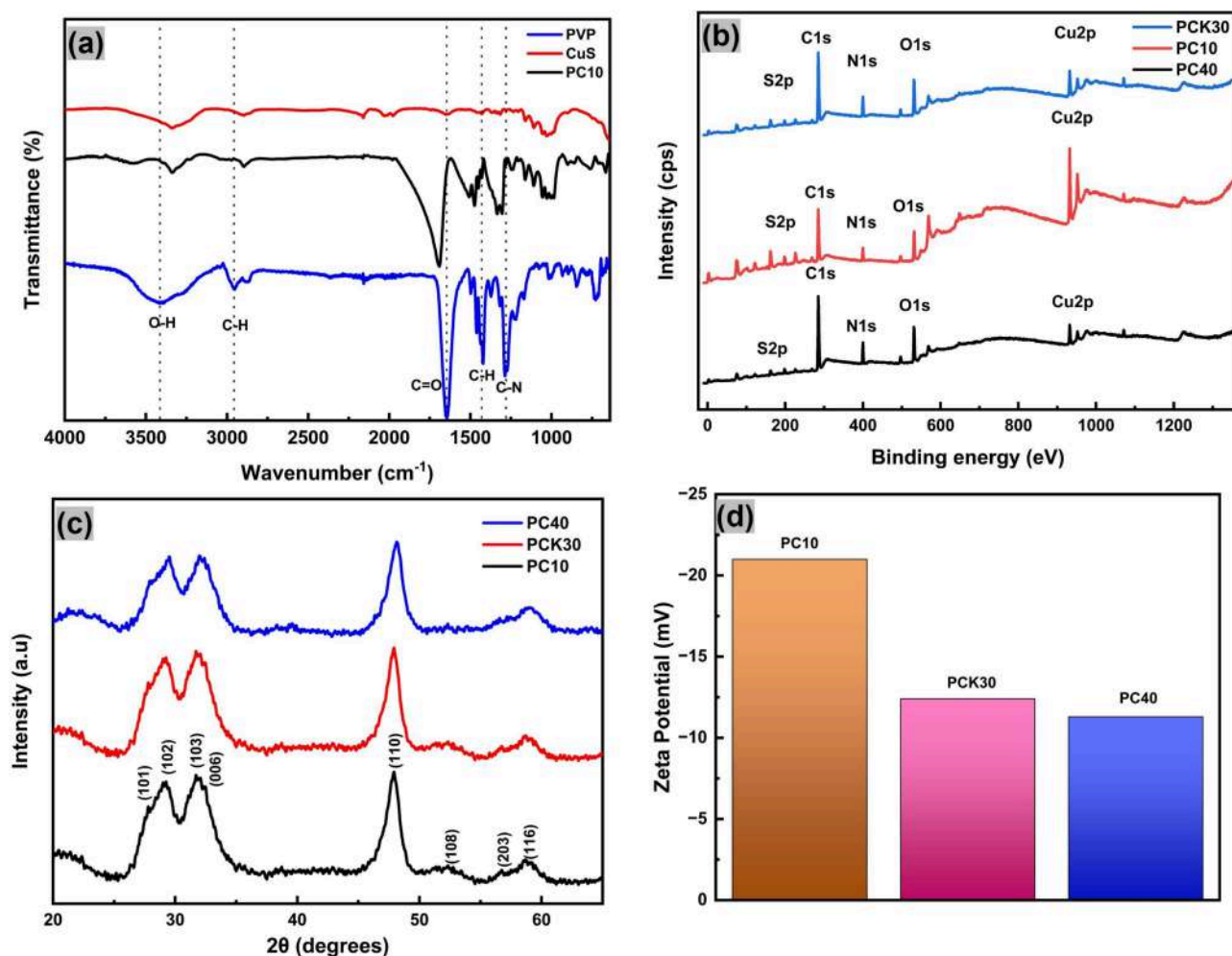


Figure 3. Characterizations of the nanoflakes: (a) FTIR spectra of PC10, CuS, and PVP displaying the shifts in the spectra of PC10 compared to PVP. (b) XPS spectrum of PC10, PC40, and PCK30 revealing the peaks of all the elements present in the particles. (c) XRD of all the three particles. (d) Zeta potential measurements of the particles

S^{2-} and Cu^{2+} and ultimately the formation of Cu_2S . The reaction proceeded for 1 h at a temperature of 110°C .

After the synthesis process was completed, TEM micrographs were captured to examine the structure and morphology of the particles, as shown in Figure 2a–c. The TEM micrographs exhibited a uniform dispersion of particles, displaying a diverse array of shapes, with a predominant presence of flake-like morphology. All particles were found to be smaller than 10 nm in size. To analyze the mean size distribution, a detailed analysis was conducted on more than 100 individual particles that exhibited no signs of aggregation. Only well-dispersed single particles were selected for the study. ImageJ software was employed to quantify the size of each particle and construct a histogram representing the distribution. The results indicated that PCK30 demonstrated the smallest mean size of 5.8 nm, as depicted in Figure 2c and f. This was followed by PC40 with a mean size of 7.5 nm (Figure 2b and e) and PC10 with a mean size of 9 nm (Figure 2a and d). The presence of longer PVP chains and a higher concentration of carbonyl groups in PCK30 compared to PC10 and PC40 provided enhanced steric stabilization, limiting crystal growth and resulting in smaller particle sizes. Further analysis using High-Resolution TEM (HR-TEM) confirmed the crystalline nature and growth of the particles.

PC10 and PC40 exhibited a hexagonal CuS phase, with crystal planes corresponding to (006) and (101), respectively, as validated by 2D Fast Fourier Transform (2D-FFT) analysis of the HR-TEM fringes. The hexagonal symmetry of CuS was evident from the presence of bright spots in the 2D-FFT of the HR-TEM fringes. Supplementary Figure S1 provides additional details of this characterization.

In order to investigate the crystal growth and phase structure planes of the synthesized particles, XRD was performed on all three particles, as illustrated in Figure 3c. The recorded peaks and associated planes at (101): 27.6° , (102): 29.17° , (103): 31.8° , (006): 32.7° , and (110): 47.8° were attributed to the hexagonal CuS phase of copper sulfide (JCPDS no. 06-0464).^{41,42} The maximum crystal growth was observed in the (110) plane, as indicated by the highest intensity peak. A broad hump near 20° was attributed to PVP. Notably, there was no evidence of any additional peaks corresponding to other stoichiometries of copper sulfide, indicating the presence of a single phase. Although all three particles showed distinct peaks that displayed the crystalline nature of CuS, the peaks exhibited by PC10 and PC40 were sharper, followed by those of PCK30 and PC40, indicating maximum crystallinity in PC10. The higher molecular weight PVP chains might have formed a thicker layer around the CuS nanoflakes, providing an

amorphous character to the particles. The absence of additional peaks of other stoichiometries demonstrated the purity of the sample. Furthermore, the XRD data correlated well with the data obtained from HR-TEM.³⁰

The electronic interactions between PVP and CuS crystals were investigated by using FTIR spectroscopy, as depicted in Figure 3a. To understand the nature of these interactions, the study focused on PC10, considering that the functional groups were similar in all three particle types. Pure PVP exhibited characteristic C=O stretching vibrations at 1644 cm⁻¹, indicating the presence of a pyrrolidone group. Additional peaks corresponding to C–N, C–H bending, O–H stretching, and C–H stretching were observed at 1283 cm⁻¹, 1422 cm⁻¹, 3409 cm⁻¹, and 2957 cm⁻¹, respectively.⁴³ Notably, in PC10, the C=O stretching band exhibited a blue shift, with the peak appearing at 1695 cm⁻¹, indicating a chemical change in the PVP structure during the synthesis process. Similarly, blue shifts were observed in the C–H and C–N peaks of PC10, suggesting the presence of ionic interactions. The observed blue shifts can be attributed to the concentration of PVP, as reported in previous studies.⁴⁴ Additionally, zeta potential measurements were performed by dispersing the colloidal suspension in phosphate buffer at pH 7, as shown in Figure 3d. PC10 displayed a colloidal surface charge of –21 mV, followed by those of PCK30 and PC40. These findings not only indicate the stability of the particles but also provide valuable insights into their fate and behavior in a biological environment. To gain a deeper understanding of the chemical and oxidation states of Cu and S, XPS measurements were conducted. The nanoflakes were redispersed in water and deposited onto a silicon wafer, which was then air-dried for analysis. Figure 3b displays the XPS spectra of all three particle types. C 1s, N 1s, and O 1s peaks were detected in all three samples, confirming the presence of PVP, which contains carbon, nitrogen, and oxygen. It was observed that the carbon intensity at 284.6 eV increased with PVP molecular weight, with PCK30 exhibiting the highest C 1s intensity due to its longer PVP chain. Conversely, PC10 had the lowest carbon intensity. Notably, Cu and S peaks were most prominent in PC10, indicating a higher percentage of Cu and S in PC10, despite the similar precursor concentrations in all samples.

The high-resolution spectra in Supplementary Figure S5 provided valuable insights into the oxidation states and elemental composition of the synthesized nanoparticles. The Cu 2p spectra exhibited binding energy peaks at 932.5 eV (Cu 2p_{3/2}) and 952.1 eV (Cu 2p_{1/2}), indicating the presence of Cu²⁺ oxidation state.⁴⁵ The observed energy difference of 20 eV between the two peaks further supported this finding. No other oxidation states of copper were detected. The S 2p scan revealed two distinct binding energy values, confirming the presence of S²⁻.³⁰ In Supplementary Figure S5, the S 2p spectrum displayed two separate peaks corresponding to the spin–orbit splitting of the S 2p_{1/2} and S 2p_{3/2} orbitals, located at 162.5 and 161.5 eV, respectively. The first peak can be attributed to S bonding with Cu, while the second peak indicates the formation of S–S dimers. The atomic percentages of the elements in the particles are provided in Table 1, revealing high atomic percentages of Cu and S in PC10. These findings provide important evidence regarding the oxidation states and chemical compositions of the synthesized nanoparticles.

To examine the optical properties of the synthesized nanoparticles, we obtained UV–vis-NIR absorbance spectra.

Table 1. Atomic Percentages of Various Elements: XPS Analysis

Sample %	C	N	O	Cu	S
PC10	58.72	7.59	13.04	9.67	11.03
PCK30	69.63	10.04	13.56	2.95	3.82
PC40	71.61	9.79	13.57	2.23	2.79

All nanoparticles displayed absorbance in the NIR range with a peak at 1020 nm, regardless of their size, indicating the formation of CuS as shown in Figure 4d. PC10 exhibited higher OD values than PC40 and PCK30, which can correlate with the XPS analysis demonstrating more CuS content in the particles. The increase in the absorbance in PC10 can also be attributed to its larger particle size. With the decreasing particle size, the band gap also decreases but we found that PCK30 had the smallest particle size, showing highest band gap, and lowest absorption (Supplementary Figure S3). The absorbance spectrum was acquired for different concentrations of the sample, and the results are presented in Supplementary Figure S2. The data clearly showed an increase in the OD values with an increasing concentration of the sample.

The Raman spectra of the nanoflakes were analyzed by drop-casting the samples onto a glass slide, and the obtained results are shown in Figure 4a. The presence of a sharp peak in the spectra indicated excellent crystallinity of the material, originating from the lattice vibrations of the covellite structure. Specifically, in PC10, a sharp peak at 470 cm⁻¹ confirmed the presence of the S–S bond stretching within the structure. A slight red-shift was observed in PC40 compared to PC10, with a peak value at 470.5 cm⁻¹, indicating an improvement in the material's crystallinity. Conversely, PCK30 exhibited a blue shift, suggesting a decrease in the material's crystallinity, with a peak value at 467 cm⁻¹. Additionally, a less intense hump at 270 cm⁻¹ was observed, which could be attributed to the vibrational energies of the Cu–S bond.⁴⁶ These findings align with previous studies on Raman spectroscopy, highlighting its effectiveness in characterizing the crystallinity and chemical composition of materials.⁴⁶

To assess the stability of the particles, zeta potential measurements were performed over a 15-day period. The results indicated only a slight decrease in the zeta potential when the colloidal solutions were stored at 4 °C, suggesting that the particles remained colloidally stable without any signs of sedimentation. To comprehend the thermal stability of the particles, TEM analysis was employed to examine potential changes in particle morphology. As depicted in Supplementary Figure S9, minimal alterations were noted in the particle morphology, and they exhibited a flake-shaped structure. It is well-documented that CuS nanoparticles undergo surface oxidation in aqueous environments, and the nature of surface coatings plays a critical role in determining the physicochemical properties of CuS nanoflakes.⁴⁷ For instance, the formation of a CuSO₄ surface layer can modify the properties of the nanoparticles, leading to increased solubility and enhanced ion dissolution while compromising their localized surface plasmon resonance (LSPR) performance. Previous studies have also highlighted the cytotoxicity of Cu ions, as they can cause damage to DNA and proteins.^{48,49} To investigate the stability of the particles from an oxidation standpoint, X-ray photoelectron spectroscopy (XPS) studies were conducted on the particles after storage for 1 and 15 days of storage. As previously mentioned, fresh CuS nanoparticles exhibit peaks

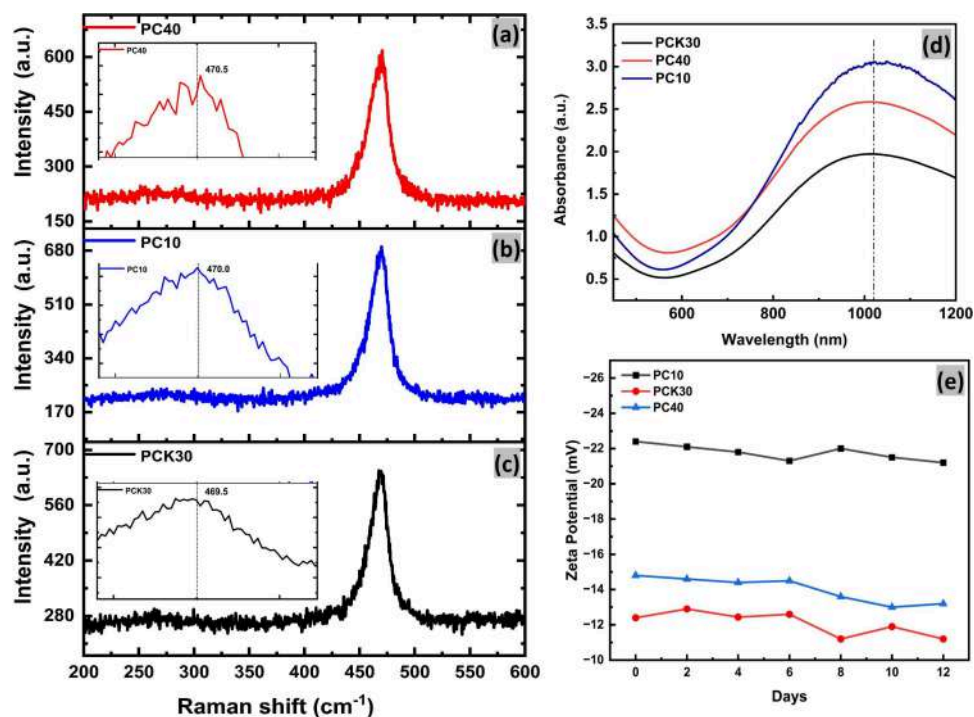


Figure 4. Optical characterization and surface charge study. (a) Raman spectra obtained for PC40. The inset image demonstrates the peak shift. (b) Raman spectra obtained for PC10. The inset image demonstrates the peak. (c) Raman spectra obtained for PCK30. The inset image demonstrates the peak shift. (d) Absorbance spectra of PC10, PC40, and PCK30 with maximum absorbance at 1020 nm. (e) Stability of surface charge conducted for 15 days via zeta potential measurements.

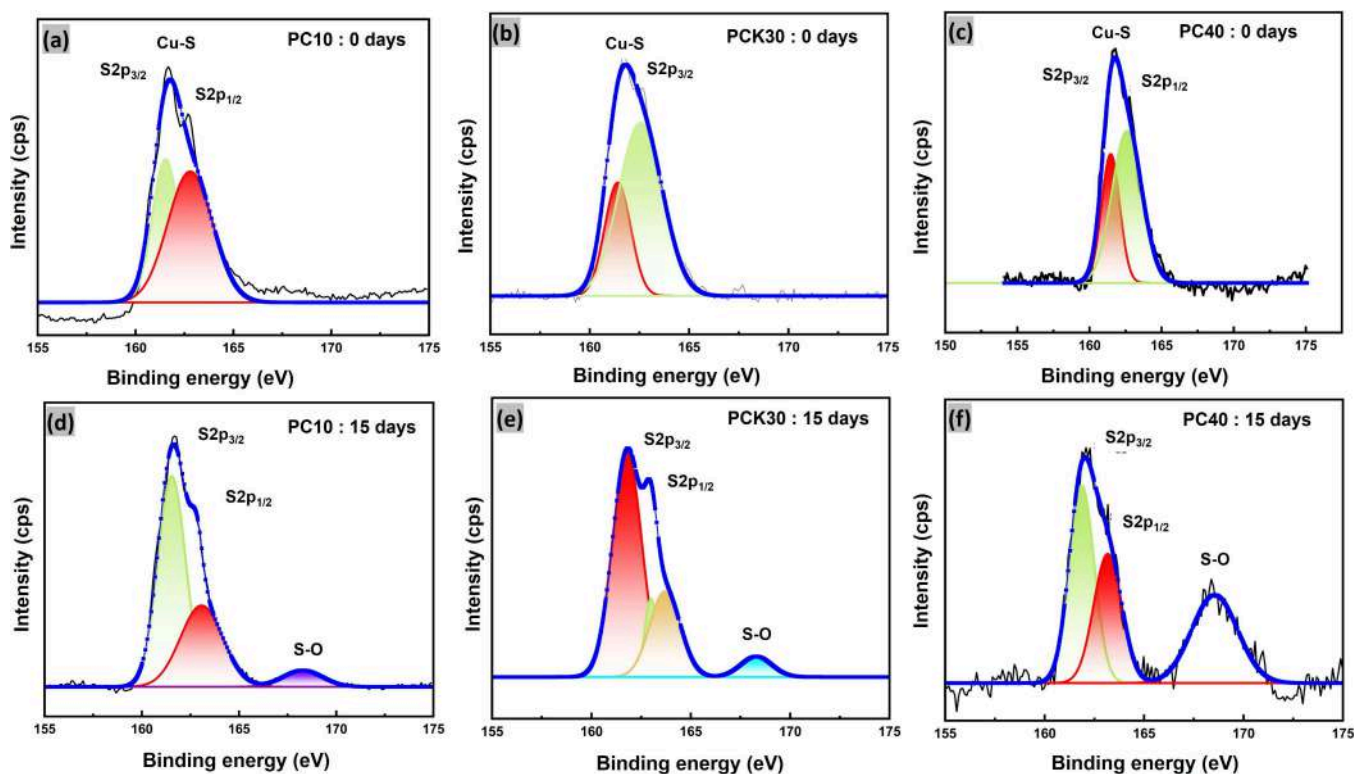


Figure 5. XPS graphs showing the sulfur oxidation states over a period of 15 days. (a) S binding energies of PC10 at day 0. (b) S binding energies of PC40 at day 0. (c) S binding energies of PCK30 at day 0. (d) S binding energies of PC10 at day 15. (e) S binding energies of PC40 at day 15. (f) S binding energies of PCK30 at day 15.

corresponding to Cu 2p and S 2p. The surface oxidation was analyzed based on the S peaks in the XPS spectra, as depicted

in Figure 5. Notably, surface oxidation leads to the formation of sulfate (S–O bond) ions with a peak binding energy of

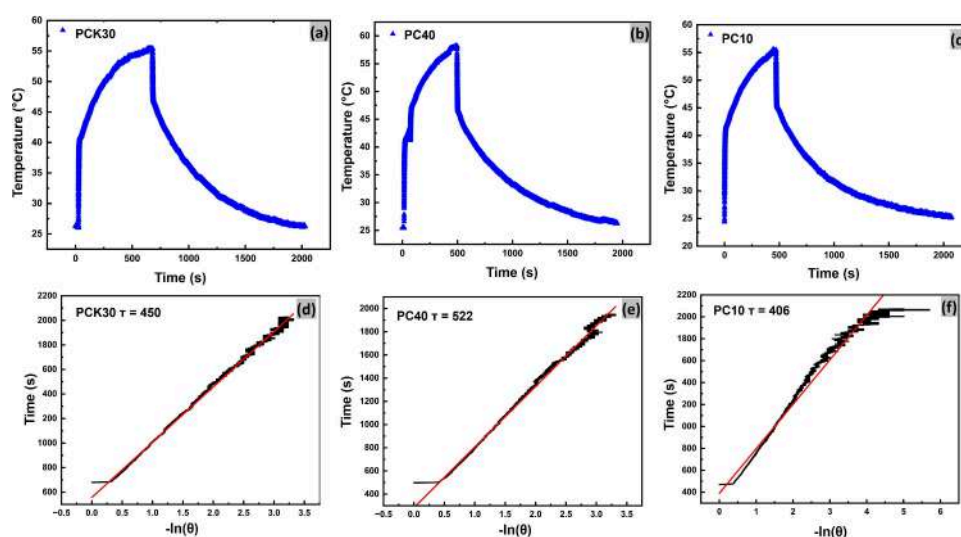


Figure 6. Photothermal efficiency calculations: (a) PCK30 heating and cooling cycle, (b) PC40 heating and cooling cycle, and (c) PC10 heating and cooling cycle. Corresponding Time vs $-\ln(\theta)$ graphs (d) PCK30 linear fit, (e) PC40 linear fit, and (f) PC10 linear fit.

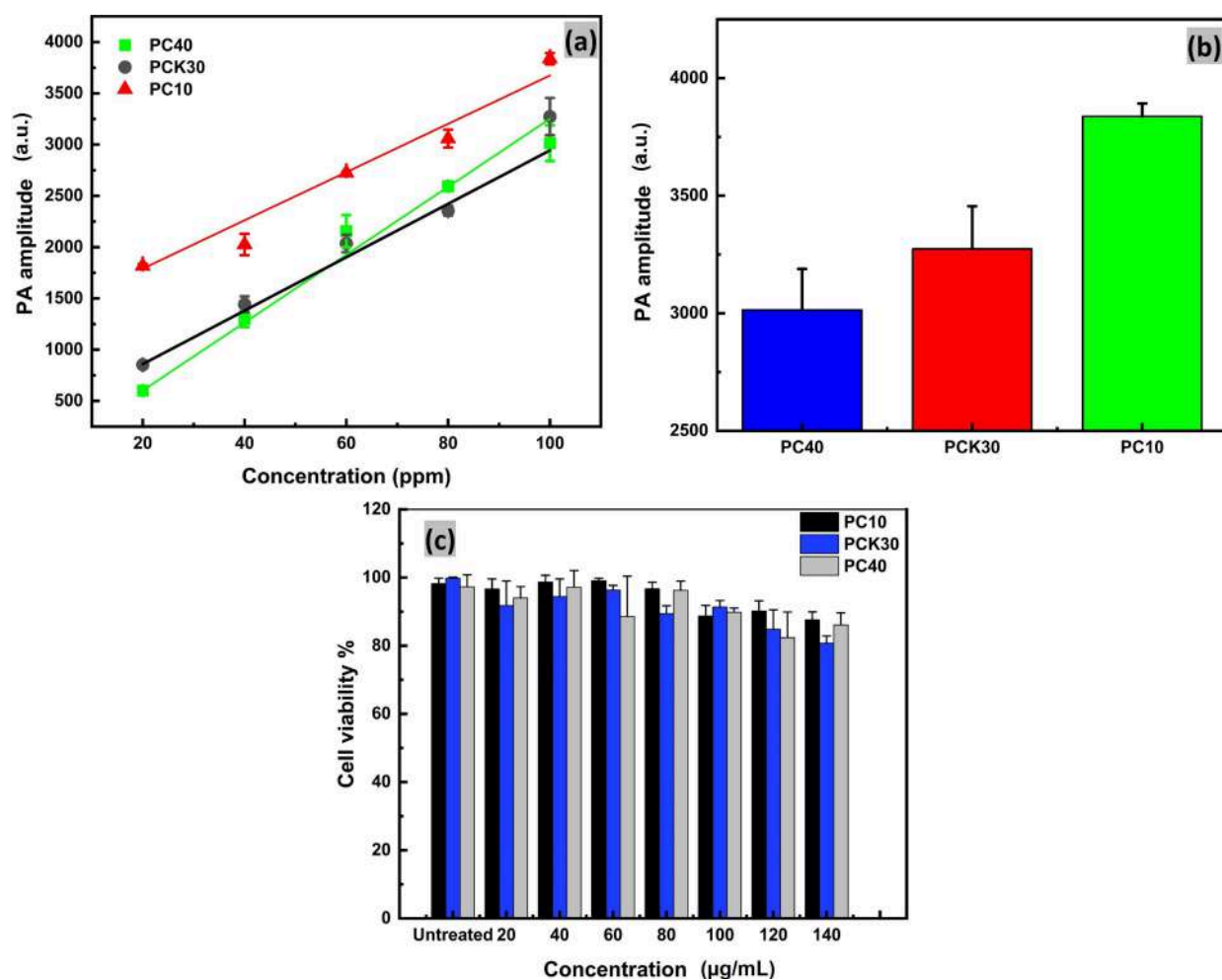


Figure 7. Photoacoustic properties and cytocompatibility: (a) Concentration-dependent PA intensity values showing linear relation. (b) PA intensity at 916 nm for PC10, PC40, and PCK30. (c) Concentration-dependent cytocompatibility studies.

169.4 eV in the S 2p region. Additionally, a peak at 164.2 eV was observed, indicating the presence of polysulfide species due to Cu-deficient regions on the surface.⁵⁰ The S 2p peak at 169.4 eV, associated with surface oxidation, was observed in all

three types of particles after storage for 15 days in an aqueous environment. The intensity of the peak related to the formation of S–O bonds was notably higher in PCK30 compared to that in PC40 and PC10. During the process, Cu

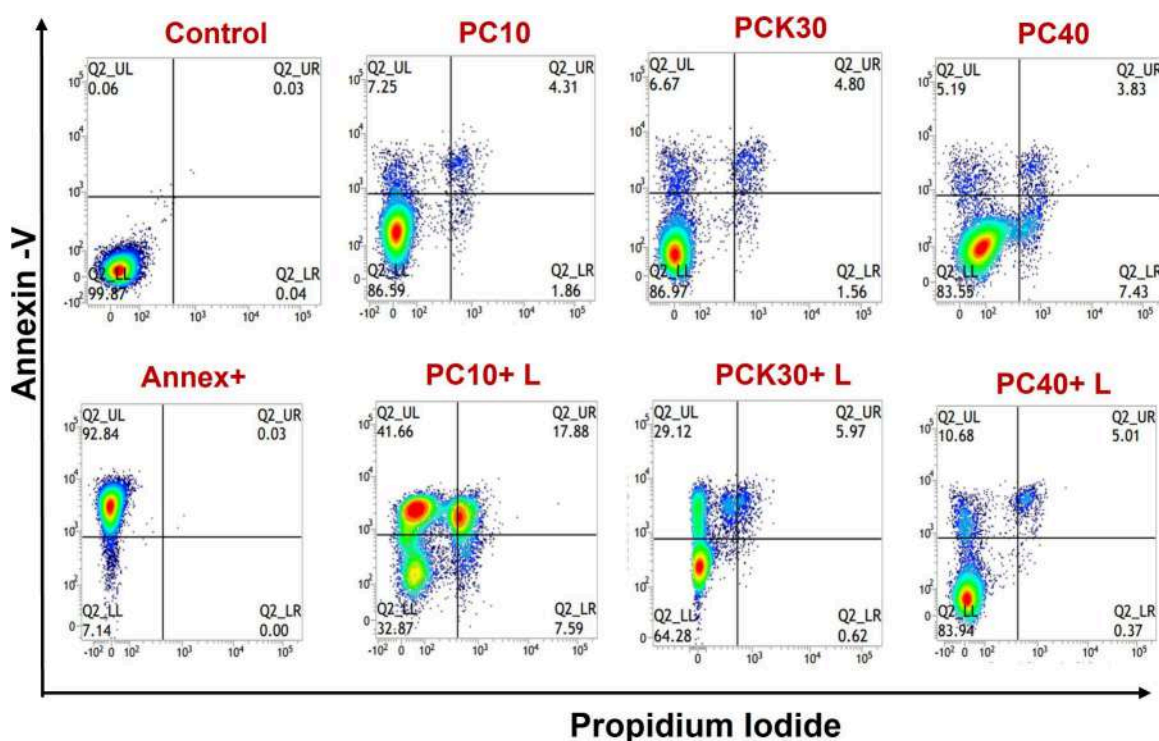


Figure 8. Apoptosis assay showing the cell population at various stages after treatment. Q2_UL in each figure represents the early apoptosis population; Q2_UR represents secondary necrosis population; Q2_LR represents the cells stained with only PI showing necrotic population. Pictorial represents comparative analysis of population treated with samples with and without laser irradiation for 5 min at the 6th hour and the 12th hour.

ions leached into the solution, resulting in the formation of copper-deficient regions on the particle surface. [Supplementary Figure S4](#) presents the atomic percentages of various elements on the first and 15th days, revealing an increase in the atomic percentage of O 1s and a decrease in the percentage of Cu on the 15th day.

The synthesized nanoparticles, PC10, PCK30, and PC40, exhibit a diverse range of structural and optical properties. The HR-TEM, XRD, and Raman spectra analyses reveal that PC10 has the highest degree of crystallinity among the three particles. Moreover, XPS investigations demonstrate that PC10 contains a higher percentage of Cu compared with the other particles. The elevated absorbance value of PC10 can be ascribed to its superior crystallinity, greater Cu percentage, larger size, and lower band gap.

3.2. Photothermal Studies. The synthesized nanoflakes exhibited remarkable optical properties with strong absorbance in the NIR range, leading us to investigate their photothermal conversion efficiency (η). To this end, an aqueous solution of the particles was subjected to irradiation with 1064 nm continuous wave laser light of 1 W power for 500 s, followed by a cooling cycle. A plot showing the temperature variation with time was recorded during the continuous irradiation of a sample until it attained a stable temperature, and subsequently, the laser was turned off. Upon light irradiation, a rapid increase in temperature was observed, as depicted in [Figure 6](#). The photothermal efficiency (η) was calculated using Roper's method with modifications explained in the [Supporting Information](#).⁵¹ To determine the system time constant (τ_s), we introduced a parameter θ , defined as follows:

$$\theta = \frac{T - T_{\text{Surr}}}{T_{\text{Max}} - T_{\text{Surr}}}$$

$$t = -\tau_s \ln(\theta)$$

where T is the temperature, T_{Surr} is the surrounding temperature, T_{Max} is the maximum temperature, and t is the time. PC10 exhibited the highest η value of 51%, followed by PC40 with 38%, and PCK30 with 44%. The efficiency obtained by the particles are comparable to other reported studies.^{52–55} These results suggest that among the synthesized nanoparticles, PC10 has a high potential for applications as photothermal therapy agents for both in vitro and in vivo studies compared to the other two types of particles. The particles exhibited robust performance even after undergoing four cycles of heating and natural cooling, affirming their high photothermal stability, as illustrated in [Supplementary Figure S8](#).

3.3. Photoacoustic Properties. To investigate the photoacoustic properties of the nanoflakes, we employed phantom-based multispectral optoacoustic tomography (MSOT) imaging was employed. As mentioned earlier, the nanoflakes exhibited a maximum absorbance at 980 nm. The photoacoustic spectra of the particles at various concentrations were measured in a tissue-mimicking phantom, as depicted in [Figure 7a](#) and [Supplementary Figure S6](#). Intriguingly, the photoacoustic spectra of the particles exhibited a blue shift in comparison to that of the absorbance maxima. This observation is reminiscent of a previous study that reported a similar blue shift when analyzing the photoacoustic signal changes related to Ca^{2+} dependence.⁵⁶ [Supplementary Figure S7](#) shows the plot of photoacoustic intensity as a function of wavelength, indicating that all particles demonstrated max-

imum photoacoustic intensity at 916 nm, which was inconsistent with the absorbance peak. Normally, the photoacoustic and absorbance peaks of particles should align since both are based on the same principle of absorption. However, in our case, the difference could be attributed to the decreased laser power at higher near-infrared (NIR) wavelengths.⁵⁷ It is important to consider that water exhibits an absorption peak at 980 nm, with the onset of absorption occurring at wavelengths as low as 910 nm. This becomes particularly relevant when the MSOT system is used for phantom measurements, as the system involves a water-filled chamber. It is important to consider that when using laser irradiation on phantoms wavelengths beyond 910 nm can be influenced by the presence of water in the chamber. This is because water begins to absorb laser light at this particular wavelength. Considering this, it is reasonable to assume that if similar particles are used inside the body, they might experience a similar interference pattern due to the presence of water in biological tissues. However, through spectral unmixing, which is a capability of MSOT analysis, it is possible to separate the water signal from the phantom signal.

Furthermore, as shown in Figure 7a, the particles exhibited linear photoacoustic growth at 916 nm with an increase in the particle concentration. The correlation coefficients (R^2 values) were greater than 0.98 for PC10, PC40, and PCK30, indicating a strong linear relationship between the photoacoustic intensity and the particle concentration. Among the particles, PC10 displayed the highest photoacoustic intensity, followed by PCK30 and PC40, as depicted in Figure 7b. These photoacoustic properties were consistent with the other observed properties of the particles in this study. The small size of these particles suggests their potential application as photoacoustic contrast agents, which could enable deep tumor contrast imaging. By utilizing their strong photoacoustic signal, these particles may aid in the detection and visualization of tumors in deep tissues, offering promising prospects for biomedical imaging applications.

3.4. Cytocompatibility and Apoptosis Studies. Cytotoxicity investigations were carried out on the A549 lung cancer cell line to assess the potential harm caused by the prepared nanoflakes at various concentrations ranging from 20 $\mu\text{g/mL}$ to 140 $\mu\text{g/mL}$. The cytocompatibility of the nanoflakes was evaluated using the MTT assay, following a 24 h incubation period with the cells. Encouragingly, the results revealed no observable toxicity, even at the highest concentration tested (140 $\mu\text{g/mL}$), as illustrated in Figure 7c. This experiment was repeated to ensure the reliability of the findings, and similar outcomes were obtained. Moreover, apoptosis studies were conducted using comparable concentrations of the nanoflakes as shown in Figure 8. The aim was to investigate whether the nanoflakes, when exposed to laser irradiation, possessed the capability to induce apoptosis in the cells. To this end, Annexin-FITC-PI studies were performed. By analyzing the effects of the particles postlaser irradiation, their potential in triggering apoptosis could be evaluated.

In this study, flow cytometry analysis was employed to determine the proportions of apoptotic and necrotic cell populations in both treated and untreated cells. This approach allowed for a comprehensive understanding of the different stages of apoptosis occurring in the cells. Annexin V-FITC conjugation was utilized to detect early apoptotic cells by specifically binding to phosphatidyl serine (PS) residues exposed on the outer leaflet of the plasma membrane during

the early stages of apoptosis. Propidium iodide (PI), which is impermeable to intact membranes, was used to identify necrotic and late apoptotic cells with compromised plasma membranes. Live cells were stained with Annexin V and excluded from PI staining. At the late stage of apoptosis, cells were conjugated with Annexin V-FITC and exhibited bright PI staining.

Flow cytometry results demonstrated that apoptosis was the predominant pathway observed in all cases, with only a small percentage of cells undergoing necrosis. Treatment with laser irradiation resulted in a higher percentage of apoptotic cells compared to that treated without laser irradiation. Notably, the highest overall cell death (67.13%) was observed in PC10-treated cells subjected to 5 min of laser irradiation, whereas PC40 showed the least effect, with only 16.05% cell death. PCK30 exhibited a moderate response with 35.7% cell death. It is worth highlighting that in all instances the proportion of secondarily necrotic cells increased following laser irradiation. The apoptosis was the primary mode of cell death, and the necrotic population remained relatively low. These findings indicate that the utilization of these nanoflakes in therapeutic applications could potentially mitigate tissue damage associated with necrosis. Thus, PC10 nanoflakes show promise for effective implementation in photothermal therapy with the necessary modifications.

4. CONCLUSION

Rising cancer cases demand innovative approaches for effective treatment. Therefore, combined theranostic strategies are necessary to address these challenges. In this regard, we developed PVP-capped nanoparticles with various molecular weights of PVP, presenting distinct properties. These nanoparticles can be used for theranostic systems that combine photothermal therapy and photoacoustic effects. Our studies revealed that the synthesized nanoparticles were smaller than 10 nm and exhibited crystalline properties. All nanoparticles had an absorbance peak at 980 nm, indicating their potential for generating good photoacoustic and photothermal responses. Photoacoustic absorption correlated well with the absorbance spectra until 916 nm but deviated afterward. Among all of the nanoparticles, PC10 showed the best photoacoustic property, and linearity was observed with increased concentrations. Photothermal experiments showed a temperature increase in all cases, with PC10 exhibiting an efficiency of 51%. Cytotoxicity assays revealed that the nanoparticles were compatible with the cells. The treated cells showed a higher incidence of apoptosis than necrosis, suggesting that the treatment would elicit a lower immune response in the tissue. We also observed a higher cell death rate of up to 67% in cells treated with nanoparticles, followed by laser irradiation, indicating the efficacy of photothermal therapy. In conclusion, our study highlights the potential of PVP-capped nanoparticles in combined theranostic strategies for cancer treatment. Among the synthesized nanoparticles, PC10 demonstrated superior photoacoustic and photothermal properties and exhibited better stability, making it a suitable candidate for cancer therapy.

However, to establish the credibility of these nanoparticles further, several additional studies need to be conducted. Our research also encountered some challenges during the synthesis process. The particle size of the nanoparticles was highly dependent on the reaction temperature, and the reaction had to be terminated at specific times to obtain

uniform particle sizes. Moreover, a significant limitation of these nanoparticles is that they cannot be covalently conjugated easily as it requires a lengthy process of chain-opening reactions, and biofunctionalization can only be achieved through adsorption. Nonetheless, further studies are necessary to optimize their properties and address the challenges faced during the synthesis process. Overall, our research provides a valuable contribution to developing PVP-capped ultrasmall nanoparticles for therapy and imaging.

■ ASSOCIATED CONTENT

SI Supporting Information

The Supporting Information is available free of charge at <https://pubs.acs.org/doi/10.1021/acsabm.3c01123>.

Characterizations, transmission electron microscopy, optical characterizations, XPS-based stability test, and photothermal cycle (PDF)

■ AUTHOR INFORMATION

Corresponding Authors

Sanhita Sinharay – Centre for Biosystems Science and Engineering, Indian Institute of Science, Bangalore 560012, India; orcid.org/0000-0001-9910-996X; Email: sanhitas@iisc.ac.in

Ashok M. Raichur – Department of Materials Engineering, Indian Institute of Science, Bangalore 560012, India; College of Science, Engineering and Technology, University of South Africa, Johannesburg 1709, South Africa; orcid.org/0000-0001-5042-3122; Email: amr@iisc.ac.in

Authors

Madhavi Tripathi – Department of Materials Engineering, Indian Institute of Science, Bangalore 560012, India; orcid.org/0000-0002-4736-9134

Ananya Sharma – Centre for Biosystems Science and Engineering, Indian Institute of Science, Bangalore 560012, India

Complete contact information is available at: <https://pubs.acs.org/10.1021/acsabm.3c01123>

Notes

The authors declare no competing financial interest.

■ ACKNOWLEDGMENTS

Sanhita Sinharay would like to acknowledge the support from SERB research grant and R.I. Mazumdar Young Investigator award.

■ REFERENCES

- (1) Heiss, J. D.; Lungu, C.; Hammoud, D. A.; Herscovitch, P.; Ehrlich, D. J.; Argersinger, D. P.; Sinharay, S.; Scott, G.; Wu, T.; Federoff, H. J.; et al. Trial of magnetic resonance-guided putaminal gene therapy for advanced Parkinson's disease. *Movement Disorders* **2019**, *34*, 1073–1078.
- (2) Bhaskar, S.; Tian, F.; Stoeger, T.; Kreyling, W.; de la Fuente, J. M.; Grazú, V.; Borm, P.; Estrada, G.; Ntziachristos, V.; Razansky, D. Multifunctional Nanocarriers for diagnostics, drug delivery and targeted treatment across blood-brain barrier: perspectives on tracking and neuroimaging. *Particle and fibre toxicology* **2010**, *7*, 1–25.
- (3) Moghiseh, M.; Searle, E.; Dixit, D.; Kim, J.; Dong, Y. C.; Cormode, D. P.; Butler, A.; Gieseg, S. P. Spectral Photon-Counting CT Imaging of Gold Nanoparticle Labelled Monocytes for Detection of Atherosclerosis: A Preclinical Study. *Diagnostics* **2023**, *13*, 499.
- (4) Ge, J.; Jia, Q.; Liu, W.; Guo, L.; Liu, Q.; Lan, M.; Zhang, H.; Meng, X.; Wang, P. Red-emissive carbon dots for fluorescent, photoacoustic, and thermal theranostics in living mice. *Adv. Mater.* **2015**, *27*, 4169–4177.
- (5) Lin, H.; Chen, Y.; Shi, J. Nanoparticle-triggered in situ catalytic chemical reactions for tumour-specific therapy. *Chem. Soc. Rev.* **2018**, *47*, 1938–1958.
- (6) Cai, Y.; Chen, X.; Si, J.; Mou, X.; Dong, X. All-in-One Nanomedicine: Multifunctional Single-Component Nanoparticles for Cancer Theranostics. *Small* **2021**, *17*, 2103072.
- (7) Attia, A. B. E.; Balasundaram, G.; Moothanchery, M.; Dinis, U.; Bi, R.; Ntziachristos, V.; Olivo, M. A review of clinical photoacoustic imaging: Current and future trends. *Photoacoustics* **2019**, *16*, 100144.
- (8) Steinberg, I.; Huland, D. M.; Vermesh, O.; Frostig, H. E.; Tummers, W. S.; Gambhir, S. S. Photoacoustic clinical imaging. *Photoacoustics* **2019**, *14*, 77–98.
- (9) Qiu, T.; Lan, Y.; Gao, W.; Zhou, M.; Liu, S.; Huang, W.; Zeng, S.; Pathak, J. L.; Yang, B.; Zhang, J. Photoacoustic imaging as a highly efficient and precise imaging strategy for the evaluation of brain diseases. *Quantitative Imaging in Medicine and Surgery* **2021**, *11*, 2169.
- (10) Zeng, Y.; Dou, T.; Ma, L.; Ma, J. Biomedical Photoacoustic Imaging for Molecular Detection and Disease Diagnosis: "Always-On" and "Turn-On" Probes. *Advanced Science* **2022**, *9*, 2202384.
- (11) Liu, Y.; Bhattarai, P.; Dai, Z.; Chen, X. Photothermal therapy and photoacoustic imaging via nanotheranostics in fighting cancer. *Chem. Soc. Rev.* **2019**, *48*, 2053–2108.
- (12) Sapsford, K. E.; Algar, W. R.; Berti, L.; Gemmill, K. B.; Casey, B. J.; Oh, E.; Stewart, M. H.; Medintz, I. L. Functionalizing nanoparticles with biological molecules: developing chemistries that facilitate nanotechnology. *Chem. Rev.* **2013**, *113*, 1904–2074.
- (13) Ulbrich, K.; Hola, K.; Subr, V.; Bakandritsos, A.; Tucek, J.; Zboril, R. Targeted drug delivery with polymers and magnetic nanoparticles: covalent and noncovalent approaches, release control, and clinical studies. *Chem. Rev.* **2016**, *116*, 5338–5431.
- (14) Wang, S.; Liu, K.; Wang, F.; Peng, F.; Tu, Y. The Application of Micro-and Nanomotors in Classified Drug Delivery. *Chemistry—An Asian Journal* **2019**, *14*, 2336–2347.
- (15) Pulakkat, S.; Balaji, S. A.; Rangarajan, A.; Raichur, A. M. Surface engineered protein nanoparticles with hyaluronic acid based multilayers for targeted delivery of anticancer agents. *ACS Appl. Mater. Interfaces* **2016**, *8*, 23437–23449.
- (16) Dolai, J.; Mandal, K.; Jana, N. R. Nanoparticle size effects in biomedical applications. *ACS Applied Nano Materials* **2021**, *4*, 6471–6496.
- (17) Kobayashi, K.; Wei, J.; Iida, R.; Ijio, K.; Niikura, K. Surface engineering of nanoparticles for therapeutic applications. *Polym. J.* **2014**, *46*, 460–468.
- (18) Ahmad Nor, Y.; Niu, Y.; Karmakar, S.; Zhou, L.; Xu, C.; Zhang, J.; Zhang, H.; Yu, M.; Mahony, D.; Mitter, N.; et al. Shaping nanoparticles with hydrophilic compositions and hydrophobic properties as nanocarriers for antibiotic delivery. *ACS central science* **2015**, *1*, 328–334.
- (19) Medintz, I. L.; Uyeda, H. T.; Goldman, E. R.; Mattoussi, H. Quantum dot bioconjugates for imaging, labelling and sensing. *Nature materials* **2005**, *4*, 435–446.
- (20) van der Stam, W.; Berends, A. C.; de Mello Donega, C. Prospects of colloidal copper chalcogenide nanocrystals. *ChemPhysChem* **2016**, *17*, 559–581.
- (21) Zhao, Y.; Chen, B.-Q.; Kankala, R. K.; Wang, S.-B.; Chen, A.-Z. Recent advances in combination of copper chalcogenide-based photothermal and reactive oxygen species-related therapies. *ACS Biomaterials Science & Engineering* **2020**, *6*, 4799–4815.
- (22) Liu, K.; Liu, K.; Liu, J.; Ren, Q.; Zhao, Z.; Wu, X.; Li, D.; Yuan, F.; Ye, K.; Li, B. Copper chalcogenide materials as photothermal agents for cancer treatment. *Nanoscale* **2020**, *12*, 2902–2913.
- (23) Goel, S.; Chen, F.; Cai, W. Synthesis and biomedical applications of copper sulfide nanoparticles: from sensors to theranostics. *Small* **2014**, *10*, 631–645.

- (24) Ku, G.; Zhou, M.; Song, S.; Huang, Q.; Hazle, J.; Li, C. Copper sulfide nanoparticles as a new class of photoacoustic contrast agent for deep tissue imaging at 1064 nm. *ACS Nano* **2012**, *6*, 7489–7496.
- (25) Marin, R.; Skripka, A.; Besteiro, L. V.; Benayas, A.; Wang, Z.; Govorov, A. O.; Canton, P.; Vetrone, F. Highly efficient copper sulfide-based near-infrared photothermal agents: exploring the limits of macroscopic heat conversion. *Small* **2018**, *14*, 1803282.
- (26) Shi, S.; Wen, X.; Li, T.; Wen, X.; Cao, Q.; Liu, X.; Liu, Y.; Pagel, M. D.; Li, C. Thermosensitive biodegradable copper sulfide nanoparticles for real-time multispectral optoacoustic tomography. *ACS applied bio materials* **2019**, *2*, 3203–3211.
- (27) Neelgund, G. M.; Oki, A.; Bandara, S.; Carson, L. Photothermal effect and cytotoxicity of CuS nanoflowers deposited over folic acid conjugated nanographene oxide. *J. Mater. Chem. B* **2021**, *9*, 1792–1803.
- (28) Mutalik, C.; Okoro, G.; Krisnawati, D. I.; Jazidie, A.; Rahmawati, E. Q.; Rahayu, D.; Hsu, W.-T.; Kuo, T.-R. Copper sulfide with morphology-dependent photodynamic and photothermal antibacterial activities. *J. Colloid Interface Sci.* **2022**, *607*, 1825–1835.
- (29) Ain, N. u.; Abdul Nasir, J.; Khan, Z.; Butler, I. S.; Rehman, Z. Copper sulfide nanostructures: Synthesis and biological applications. *RSC Adv.* **2022**, *12*, 7550–7567.
- (30) Pejaj, B.; Reddivari, M.; Kotte, T. R. R. Phase controllable synthesis of CuS nanoparticles by chemical co-precipitation method: effect of copper precursors on the properties of CuS. *Mater. Chem. Phys.* **2020**, *239*, 122030.
- (31) Laurent, S.; Forge, D.; Port, M.; Roch, A.; Robic, C.; Vander Elst, L.; Muller, R. N. Magnetic iron oxide nanoparticles: synthesis, stabilization, vectorization, physicochemical characterizations, and biological applications. *Chem. Rev.* **2008**, *108*, 2064–2110.
- (32) Gao, W.; Sun, Y.; Cai, M.; Zhao, Y.; Cao, W.; Liu, Z.; Cui, G.; Tang, B. Copper sulfide nanoparticles as a photothermal switch for TRPV1 signaling to attenuate atherosclerosis. *Nat. Commun.* **2018**, *9*, 231.
- (33) Cao, F.; Wu, L.; Zhang, X.; Li, S.; Wang, C.; Zhen, W.; Jiang, X. Dynamic surface properties of PEG-coated CuS nanoparticles alter their interaction with cells as revealed by surface-enhanced infrared spectroscopy. *Nanoscale Advances* **2019**, *1*, 4268–4276.
- (34) Li, Q.-L.; Sun, Y.; Ren, L.; Wang, X.; Wang, C.; Li, L.; Yang, Y.-W.; Yu, X.; Yu, J. Supramolecular nanosystem based on pillararene-capped CuS nanoparticles for targeted chemo-photothermal therapy. *ACS Appl. Mater. Interfaces* **2018**, *10*, 29314–29324.
- (35) Zhang, C.; Fu, Y.-Y.; Zhang, X.; Yu, C.; Zhao, Y.; Sun, S.-K. BSA-directed synthesis of CuS nanoparticles as a biocompatible photothermal agent for tumor ablation in vivo. *Dalton Transactions* **2015**, *44*, 13112–13118.
- (36) Lu, G.; Li, S.; Guo, Z.; Farha, O. K.; Hauser, B. G.; Qi, X.; Wang, Y.; Wang, X.; Han, S.; Liu, X.; et al. Imparting functionality to a metal–organic framework material by controlled nanoparticle encapsulation. *Nature Chem.* **2012**, *4*, 310–316.
- (37) Koczur, K. M.; Mourdikoudis, S.; Polavarapu, L.; Skrabalak, S. E. Polyvinylpyrrolidone (PVP) in nanoparticle synthesis. *Dalton transactions* **2015**, *44*, 17883–17905.
- (38) An, L.; Wang, C.; Feng, Q.; Xu, Z.; Tian, Q.; Chai, W.; Yang, S.; Bian, Z. A flexible copper sulfide composite membrane with tunable plasmonic resonance absorption for near-infrared light-driven seawater desalination. *Environmental Science: Advances* **2022**, *1*, 110–120.
- (39) R, G.; S, R. P.; Thomas, A.; Rengan, A. K. Doxorubicin loaded polyvinylpyrrolidone-copper sulfide nanoparticles enabling mucoadhesiveness and chemo-photothermal synergism for effective killing of breast cancer cells. *Materialia* **2021**, *19*, 101195.
- (40) Bu, X.; Zhou, D.; Li, J.; Zhang, X.; Zhang, K.; Zhang, H.; Yang, B. Copper sulfide self-assembly architectures with improved photothermal performance. *Langmuir* **2014**, *30*, 1416–1423.
- (41) Mamiyev, Z. Q.; Balayeva, N. O. CuS nanoparticles synthesized by a facile chemical route under different pH conditions. *Mendelev Commun.* **2016**, *26*, 235–237.
- (42) Tripathi, M.; Padmanabhan, S.; Prakash, J.; Raichur, A. M. Seed-mediated galvanic synthesis of CuS–Au nanohybrids for phototheranostic applications. *ACS Applied Nano Materials* **2023**, *6*, 14861–14875.
- (43) Borodko, Y.; Habas, S. E.; Koebel, M.; Yang, P.; Frei, H.; Somorjai, G. A. Probing the Interaction of Poly (vinylpyrrolidone) with Platinum Nanocrystals by UV- Raman and FTIR. *J. Phys. Chem. B* **2006**, *110*, 23052–23059.
- (44) Safo, I.; Werheid, M.; Dosche, C.; Oezaslan, M. The role of polyvinylpyrrolidone (PVP) as a capping and structure-directing agent in the formation of Pt nanocubes. *Nanoscale Advances* **2019**, *1*, 3095–3106.
- (45) Kumar, P.; Nagarajan, R.; Sarangi, R. Quantitative X-ray absorption and emission spectroscopies: electronic structure elucidation of Cu 2 S and CuS. *Journal of Materials Chemistry C* **2013**, *1*, 2448–2454.
- (46) Minceva-Sukarova, B.; Najdoski, M.; Grozdanov, I.; Chunnillall, C. Raman spectra of thin solid films of some metal sulfides. *Journal of molecular structure* **1997**, *410*, 267–270.
- (47) Wu, H.; Or, V. W.; Gonzalez-Calzada, S.; Grassian, V. H. CuS nanoparticles in humid environments: adsorbed water enhances the transformation of CuS to CuSO 4. *Nanoscale* **2020**, *12*, 19350–19358.
- (48) Pham, A. N.; Xing, G.; Miller, C. J.; Waite, T. D. Fenton-like copper redox chemistry revisited: Hydrogen peroxide and superoxide mediation of copper-catalyzed oxidant production. *Journal of catalysis* **2013**, *301*, 54–64.
- (49) Wei, T.; Liu, Y.; Dong, W.; Zhang, Y.; Huang, C.; Sun, Y.; Chen, X.; Dai, N. Surface-dependent localized surface plasmon resonances in CuS nanodisks. *ACS Appl. Mater. Interfaces* **2013**, *5*, 10473–10477.
- (50) Folmer, J.; Jellinek, F. The valence of copper in sulphides and selenides: An X-ray photoelectron spectroscopy study. *Journal of the Less Common Metals* **1980**, *76*, 153–162.
- (51) Roper, D. K.; Ahn, W.; Hoepfner, M. Microscale heat transfer transduced by surface plasmon resonant gold nanoparticles. *J. Phys. Chem. C* **2007**, *111*, 3636–3641.
- (52) Yang, W.; Guo, W.; Le, W.; Lv, G.; Zhang, F.; Shi, L.; Wang, X.; Wang, J.; Wang, S.; Chang, J.; et al. Albumin-bioinspired Gd: CuS nanotheranostic agent for in vivo photoacoustic/magnetic resonance imaging-guided tumor-targeted photothermal therapy. *ACS Nano* **2016**, *10*, 10245–10257.
- (53) Zhang, B.; Wang, X.; Liu, F.; Cheng, Y.; Shi, D. Effective reduction of nonspecific binding by surface engineering of quantum dots with bovine serum albumin for cell-targeted imaging. *Langmuir* **2012**, *28*, 16605–16613.
- (54) Liu, X.; Ren, Q.; Fu, F.; Zou, R.; Wang, Q.; Xin, G.; Xiao, Z.; Huang, X.; Liu, Q.; Hu, J. CuS@mSiO 2-PEG core–shell nanoparticles as a NIR light responsive drug delivery nanoplatform for efficient chemo-photothermal therapy. *Dalton Transactions* **2015**, *44*, 10343–10351.
- (55) Liu, X.; Li, B.; Fu, F.; Xu, K.; Zou, R.; Wang, Q.; Zhang, B.; Chen, Z.; Hu, J. Facile synthesis of biocompatible cysteine-coated CuS nanoparticles with high photothermal conversion efficiency for cancer therapy. *Dalton Transactions* **2014**, *43*, 11709–11715.
- (56) Roberts, S.; Seeger, M.; Jiang, Y.; Mishra, A.; Sigmund, F.; Stelzl, A.; Lauri, A.; Symvoulidis, P.; Rolbieski, H.; Preller, M.; et al. Calcium sensor for photoacoustic imaging. *J. Am. Chem. Soc.* **2018**, *140*, 2718–2721.
- (57) Wang, J.; Hsu, S.-w.; Gonzalez-Pech, N.; Jhunjhunwala, A.; Chen, F.; Hariri, A.; Grassian, V.; Tao, A.; Jokerst, J. V. Copper sulfide nanodisks and nanoprisms for photoacoustic ovarian tumor imaging. *Particle & Particle Systems Characterization* **2019**, *36*, 1900171.

● Original Contribution

CHARACTERIZING VISCOELASTIC POLYVINYL ALCOHOL PHANTOMS FOR ULTRASOUND ELASTOGRAPHY

ANANYA SHARMA,* SAI GEETHA MARAPUREDDY,[†] ABHIJIT PAUL,* SAPNA R. BISHT,* MANIK KAKKAR,[‡]
 PRACHI THAREJA,[†] and KARLA P. MERCADO-SHEKHAR*

* Discipline of Biological Engineering, Indian Institute of Technology Gandhinagar, Gandhinagar, Gujarat, India; [†] Discipline of Chemical Engineering, Indian Institute of Technology Gandhinagar, Gandhinagar, Gujarat, India; and [‡] Discipline of Electrical Engineering, Indian Institute of Technology Gandhinagar, Gandhinagar, Gujarat, India

(Received 14 February 2022; revised 22 September 2022; in final form 24 September 2022)

Abstract—Ultrasound phantoms mimic the acoustic and mechanical properties of native tissues. Polyvinyl alcohol (PVA) phantoms are used extensively as models for validating ultrasound elastography approaches. However, the viscous properties of PVA phantoms have not been investigated adequately. Glycerol is a viscous liquid that has been reported to increase the speed of sound of phantoms. This study aims to assess the acoustic and viscoelastic properties of PVA phantoms and PVA mixed with glycerol at varying concentrations. The phantoms were fabricated with 10% w/v PVA in water with varying concentrations of glycerol (10%, 15% and 20% v/v) and 2% w/v silicon carbide particles as acoustic scatterers. The phantoms were subjected to either one, two, or three 24-h freeze–thaw cycles. The longitudinal sound speeds of all PVA phantoms were measured, and ranged from 1529 to 1660 m/s. Attenuation spectroscopy was performed in the range of 5 to 20 MHz. The measured attenuation followed a power-law relationship with frequency, wherein the power-law fit constants and exponents ranged from 0.02 to 0.1 dB/cm/MHz² and from 1.6 to 1.9, respectively. These results were in agreement with previous reports for soft tissues. Viscoelasticity of PVA phantoms was assessed using rheometry. The estimated values of shear modulus and viscosity using the Kelvin–Voigt and Kelvin–Voigt fractional derivative models were within the range of previously-reported tissue-mimicking phantoms and soft tissues. The number of freeze–thaw cycles were shown to alter the viscosity of PVA phantoms, even in the absence of glycerol. Scanning electron microscopy images of PVA phantoms without glycerol showed a porous hydrogel network, in contrast to those of PVA-glycerol phantoms with non-porous structure. Phantoms fabricated in this study possess tunable acoustic and viscoelastic properties within the range reported for healthy and diseased soft tissues. This study demonstrates that PVA phantoms can be manufactured with glycerol for applications in ultrasound elastography. (E-mail: karlamshekhkar@iitgn.ac.in) © 2022 World Federation for Ultrasound in Medicine & Biology. All rights reserved.

Key Words: Cryogel, Phantom, Glycerol, Acoustic attenuation, Sound speed, Elastography, Viscoelasticity.

INTRODUCTION

Tissue-mimicking phantoms are used to validate imaging approaches for quality control and clinical training purposes in ultrasound (Cournane et al. 2012; McGarry et al. 2020). Phantoms are developed to mimic the properties of native tissues. A wide variety of tissue-mimicking materials are available, which can be used to make customized phantoms that accurately mimic the properties of the tissue of interest.

Hydrogels are the most widely used ultrasonic tissue-mimicking phantoms (Cao et al. 2017; McGarry et al. 2020). Water is used as a solvent, and a natural polymer, such as agar and gelatin, or a synthetic polymer, such as polyacrylamide and polyvinyl alcohol (PVA), is used to form the matrix. Gelatin, agar and PVA gels have been employed to manufacture phantoms that are used extensively in elastography. The acoustic and elastic properties of these gels can be tuned to mimic specific tissues for applications in ultrasound imaging (Oudry et al. 2009; Cabrelli et al. 2017).

Extensive studies have been reported using ultrasound elastography to measure the elastic properties of tissue-mimicking phantoms (Oudry et al. 2009;

Address correspondence to: Karla P. Mercado-Shekhkar, Academic Block 6, Room 207, Indian Institute of Technology Gandhinagar, Gandhinagar, Gujarat, India 382355. E-mail: karlamshekhkar@iitgn.ac.in

Vieira et al. 2013; Cabrelli et al. 2017). The viscoelastic properties of phantoms are important for assessing ultrasound elastography and may also contain more diagnostic information. Only a handful of elastography studies have characterized viscoelastic phantoms. Nguyen et al. (2014) developed oil-in-gelatin phantoms using different concentrations of castor oil and gelatin. They used ultrasound shear wave elastography and determined that increasing the gelatin concentration increased the shear modulus of the phantoms, whereas increasing the castor oil concentration decreased the shear elastic modulus and increased the shear viscosity (Nguyen et al. 2014). Amador et al. (2015) developed tissue-mimicking viscoelastic gelatin phantoms, wherein they varied the concentration of Vanicream Lite (Pharmaceutical Specialties, Inc., Rochester, MN, USA) to modify the viscoelastic properties. Based on shear wave elastography, their results revealed that increasing the concentration of Vanicream increased the shear viscosity (Amador et al. 2015). Kumar et al. (2010) fabricated viscoelastic polyacrylamide gel-based phantoms with acrylamide concentrations varying from 2% to 20% (w/v). The values of storage and loss moduli obtained from frequency scans (0.5–100 Hz) were fit to three mechanical models, that is, the Maxwell, Kelvin–Voigt (KV) and Kelvin–Voigt fractional derivative (KVFD) models, to study the viscoelastic behavior of the phantoms. A large variation in the elastic modulus was observed at higher monomer concentrations. The authors suggested that a suitable concentration of monomer can be selected to fabricate viscoelastic phantoms corresponding to the tumor and the normal tissue (Kumar et al. 2010). Manickam et al. (2014) prepared agar-based tissue-mimicking phantoms with varying agar concentrations and characterized the biomechanical properties. As the agar concentration increased, the shear modulus of the phantoms increased.

Polyvinyl alcohol (PVA) gels have tunable acoustic and mechanical properties based on a freeze–thaw process (Hassan and Peppas 2000; Fromageau et al. 2003; Culjat et al. 2010). Compared with gelatin and agar phantoms, PVA gels are robust, durable (Funamoto et al. 2015) and inexpensive (Guo et al. 2019). In a recent proceedings article, Guo et al. (2019) measured the viscoelastic properties of PVA phantoms using a rotational rheometer. The storage modulus and the loss modulus of the samples were obtained, and the Voigt viscoelastic model was assumed to estimate the values of shear elasticity and shear viscosity of the PVA phantoms. The viscoelasticity results were compared with the values reported for fibrotic liver (Asbach et al. 2008; Zhu et al. 2016). The authors suggest that PVA can be used to construct viscoelastic phantoms to mimic fibrotic liver and help validate ultrasound elastography approaches (Guo et al. 2019).

To date, the feasibility of modifying the viscosity of PVA phantoms has not been investigated adequately, which is the focus of our work. We employed glycerol, a non-toxic, colorless and viscous liquid, to modulate the viscoelastic properties of PVA phantoms. Specifically, we tested whether PVA phantoms with a range of viscoelastic properties can be created using different concentrations of glycerol as an additive for evaluating ultrasound elastography approaches.

METHODS

Phantom fabrication

Cryogel phantoms were fabricated based on the protocol of Mercado-Shekhar et al. (2018). Distilled water was heated for 90 s using a 700-W microwave (NN-ST266B FDG, Panasonic, Madhya Pradesh, India) to attain a temperature of 80°C, measured using a thermometer. Polyvinyl alcohol powder (PVA, 10% w/v, Elvanol 71-30, Kuraray America, Inc., Houston, TX, USA) and silicon carbide powder (SiC, 2% w/v, 220 mesh size, 63 μm [nominal] diameter, Bangalore Fine Chemicals, Bangalore, India) were mixed into the water. Silicon carbide particles served as acoustic scatterers to control the echogenicity of phantoms (Oglat et al. 2018). Varying concentrations of glycerol (G9012, Sigma-Aldrich, Bangalore, India), either 0%, 10%, 15% or 20% v/v, were added into the mixture and stirred carefully to achieve a homogeneous solution while avoiding bubble formation. The solution was microwaved for 90 s using a 700-W microwave. The solution was heated until it reached +90°C, and the increase in temperature was monitored carefully with a thermometer. The solution was re-heated in increments of 10 s until the desired temperature was reached. The process of heating to +90°C ensured that the PVA powder dissolved completely. The solution was placed under vacuum at –1 bar or below for at least 5 min.

Further, the solution was allowed to cool to room temperature. A thin film of air bubbles was removed from the top surface of the mixture. After the mixture equilibrated to room temperature, it was poured into phantom molds. For acoustic measurements, cubes of phantoms were prepared with a thickness of 2.5 cm. For mechanical measurements, circular phantom disks 1 mm thick and 25 mm in diameter were fabricated. The mold was covered with aluminum foil to prevent evaporation of the solution.

The phantoms were placed in a +4°C refrigerator, which marked the start of the first freeze–thaw cycle. The phantoms were left in the refrigerator for 30 min. Phantoms were then removed from the refrigerator, and the temperature of the solution was measured using a thermometer to ensure that the solution was at +4°C.

Next, the phantoms were placed into a -20°C freezer and were allowed to freeze for 17.5 h. After this step, the phantoms were placed in the $+4^{\circ}\text{C}$ refrigerator again for 4 h. The phantoms were then placed on the lab bench at room temperature for 2 h, which marked the end of the first freeze–thaw cycle. Phantoms were subjected to either one, two or three freeze–thaw cycles. After the final freeze–thaw cycle, the phantoms without glycerol were stored in distilled water at room temperature, while the phantoms with 10%, 15% and 20% (v/v) glycerol were stored in the glycerol solutions containing the same glycerol concentration as the respective phantoms to prevent potential leaching of glycerol from the phantoms (Cournane *et al.* 2010).

Measurements of density and acoustic properties of phantoms

The mass of each phantom was obtained using a precision balance (SAB-203L, Scale-Tec, Vadodara, Gujarat, India). The volume of each phantom was measured using the water displacement method (Nahirnyak *et al.* 2006; Mercado-Shekhar *et al.* 2018). Phantom density was computed from these mass and volume measurements. The densities of 12 types of phantoms (3 independent samples per type) with varying glycerol concentrations (0%, 10%, 15% or 20% v/v) and number of freeze–thaw cycles (1, 2 or 3) were calculated.

The longitudinal sound speeds and attenuation coefficients of the phantoms were measured using the through-transmission substitution method (Mercado-Shekhar *et al.* 2018). The experimental setup used is depicted in Figure 1. Two single-element transducers (TXZ_0056, Precision Acoustics Ltd., Dorchester, UK) were placed coaxially facing each other in a tank filled with de-gassed, de-ionized water maintained at room temperature. The transducers had an active diameter of

10 mm, a focal distance of 40 mm and a -6-dB bandwidth of 5 to 20 MHz. Each phantom was placed between the transducers. A pulser-receiver (JSR DPR300, Imaginant Inc., Pittsford, NY, USA) produced an ultrasound impulse. The ultrasound was transmitted by one transducer and received by another transducer. The signal was amplified using a pre-amplifier, observed on the digital oscilloscope (MD03014, Tektronix Inc., Bangalore, India) and captured using a computer. The longitudinal speed of sound (c_l) in the phantom was calculated using the equation (Taghizadeh *et al.* 2017)

$$c_l = \frac{c_w}{1 + c_w \Delta t / h} \quad (1)$$

where c_w is the longitudinal sound speed in water (Greenspan and Tschiegg 1957), Δt is the difference in the ultrasound pulse arrival time with and without the phantom and h is the phantom thickness.

The frequency-dependent attenuation spectrum $\alpha(f)$ was computed using the equation (Raymond *et al.* 2014)

$$\alpha(f) = 10 \log_{10} \left(\frac{|V_{\text{ref}}(f)|^2}{|V_{\text{phantom}}(f)|^2} \right) / h \quad (2)$$

where f is the frequency, and V_{ref} and V_{phantom} are the amplitude spectra received from the voltage–time waveforms in the absence and presence of the phantom, respectively. The acoustic property measurements of 12 types of phantoms (three independent samples per type) with varying glycerol concentrations (0%, 10%, 15% or 20% v/v) and number of freeze–thaw cycles (1, 2 or 3) were measured. All density and acoustic measurements were obtained at room temperature (22°C – 25°C). The acoustic measurements were obtained within 2 min, and therefore, any diffusion of glycerol from the phantom samples into the water of the tank was assumed to be negligible.

Viscoelasticity measurements

The dynamic mechanical behavior of the phantoms (1-mm-thick samples) was measured using a stress-controlled rheometer (MCR 302, Anton Paar, Graz, Austria). A sandblasted parallel-plate geometry with 25-mm-diameter was used, maintaining a 1-mm measuring gap. Two types of oscillatory tests were performed on each sample: amplitude sweep and small amplitude frequency sweep. All tests were performed at 20°C . The sample was allowed an equilibration time of 300 s to attain the temperature of the rheometer plate before commencement of the protocol. During the amplitude sweep test, a strain (γ) scan was performed in the range 0.01% to

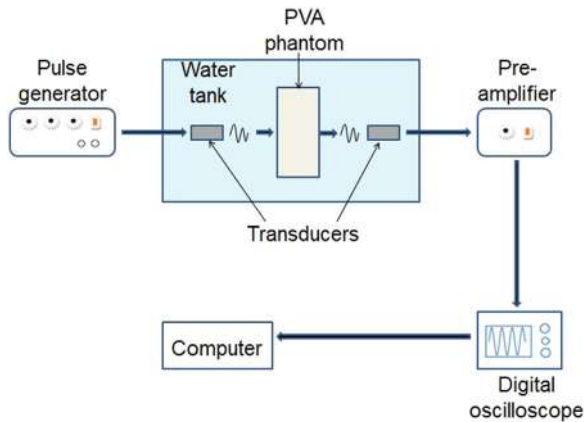


Fig. 1. Schematic of the through-transmission setup for the longitudinal sound speed and attenuation coefficient measurements. PVA = polyvinyl alcohol.

1200% strain at a frequency ω of 1 Hz (angular frequency of 6.3 rad/s). A γ of 0.5% was selected from the linear viscoelastic regime (LVR) to perform the frequency sweep in the range 1 to 16 Hz (angular frequencies of 6.3 to 100 rad/s) to calculate the storage modulus (G') and loss modulus (G''). A total of 12 types of phantoms (three independent samples per type) with varying glycerol concentrations (0%, 10%, 15% or 20% v/v) and freeze–thaw cycles (1, 2 or 3) were tested for both scan modes.

The KV and KVFD models were used to estimate the viscoelastic properties of the phantoms. These models have been reported to capture the dynamic behavior of biological soft tissues (Zhou and Zhang 2018) and are widely reported in literature (Meral et al. 2010; Parker et al. 2019; Poul and Parker 2022; Poul et al. 2022). In the KV model, the shear modulus was estimated from the storage modulus G' measurements, and the viscosity was estimated by performing a linear regression on the frequency-dependent loss modulus G'' measurements using the equation $G'' = \omega\eta$, where ω is the angular frequency and η is the viscosity (Zhou and Zhang 2018; Guo et al. 2019).

In the KVFD model, the storage and loss moduli are defined by the equations (Zhou and Zhang 2018)

$$G' = \mu_0 + \mu_a \omega^a \cos\left(\frac{\pi}{2}a\right) \quad (3)$$

$$G'' = \mu_a \omega^a \sin\left(\frac{\pi}{2}a\right) \quad (4)$$

where μ_0 (kPa) is the shear modulus, μ_a ($\text{kPa} \cdot \text{s}^a$) is related to the shear viscosity and a is the fractional order of the spring-pot element. When $a = 0$, the model behaves like a Hookean spring, whereas when $a = 1$, it acts as a dashpot. For any intermediate value of a , the model represents a fractional dashpot (Zhou and Zhang 2018; Poul et al. 2022). For fitting the KVFD model to the rheometer measurements, we followed the approach taken by Gomez et al. (2022), wherein the frequency-dependent shear wave speed (c_s) was estimated from the storage and loss modulus measurements using the equation (Gomez et al. 2022)

$$c_s(\omega) = \sqrt{\frac{2 \left(G'^2(\omega) + G''^2(\omega) \right)}{\rho \left(G'(\omega) + \sqrt{G'^2(\omega) + G''^2(\omega)} \right)}} \quad (5)$$

where ρ is the density of the phantom, which was assumed to be 1000 kg/m^3 . This approach was taken because using the shear wave speed values enabled estimation of the KVFD parameters (μ_0 , μ_a and a). Thereafter, the KVFD model (using eqns [3], [4] and [5]) was fit to the c_s values using a least-squares non-linear

regression method to estimate the shear KVFD viscoelastic parameters μ_0 , μ_a and a (Gomez et al. 2022).

Field emission scanning electron microscope analyses

The surface morphology of the phantoms was visualized with a field emission-scanning electron microscope (JEOL, JSM-7600F, Tokyo, Japan). Field emission scanning electron microscope (FE-SEM) analyses were performed to determine whether the viscoelasticity measurements were affected by the microstructural changes of the phantoms with various glycerol concentrations. In preparation for FE-SEM, phantoms 1 mm thick and 25 mm in diameter were kept overnight at -80°C . The frozen sample was further lyophilized under vacuum at -86°C for 48 h to sublime all water content. The sample was mounted on an aluminum stub with conductive tape and sputter-coated with platinum under vacuum to provide conductance. Five SEM images were captured for a total of 12 phantoms with varying glycerol concentrations (0%, 10%, 15% or 20% v/v) and different numbers of freeze–thaw cycles (1, 2 or 3). The porosity of phantoms without glycerol was measured by analyzing the SEM images using the open-source software Fiji (ImageJ 1.53 C, National Institutes of Health, Bethesda, MD, USA).

Statistical analyses

The mean and standard deviation of density and longitudinal sound speed measurements of three samples of each phantom type were computed. We verified that the replicate measurements for each experimental arm were normally distributed using the Jacque–Bera test ($p > 0.05$). The F -test was used to determine whether the data had equal or unequal variances. Independent t -tests, the non-parametric Wilcoxon sign rank test, analysis of variance and Tukey's *post hoc* multiple comparison test were used to determine whether the differences in density, longitudinal sound speed, shear modulus and viscosity estimates between phantom types were statistically significant. Correlation analysis was performed to quantify the strength of linear trends in the data. Power law regression analysis was performed on the attenuation measurements as a function of frequency, given as $\alpha(f) = \alpha_0 f^n$, wherein α_0 and n are the power law constant (dB/cm/MHz^n) and power law exponent, respectively. The coefficient of determination (R^2) was computed to determine the goodness of fit to the data. The 95% confidence bounds of the power law constants and exponents for each phantom type were computed. The mean and standard deviation of porosity for five SEM images of each phantom without glycerol were computed. Statistical tests were performed using MATLAB (R2020b, The MathWorks, Inc., Natick, MA,

USA). A p value <0.05 was used to denote significant differences for all statistical tests.

RESULTS

Density, longitudinal sound speed and attenuation measurements of phantoms

The measured densities of the phantoms are illustrated in Figure 2A and ranged from 1.12 to 1.44 g/cm³. For each glycerol concentration, no significant differences in density measurements between the numbers of freeze–thaw cycles were observed ($p = 0.32, 0.63, 0.092$ and 0.087 for 0%, 10%, 15% and 20% glycerol, respectively). Further, for the phantoms that underwent one and two freeze–thaw cycles, no significant differences in density measurements between glycerol concentrations were observed ($p = 0.47$ and 0.20 for one and two freeze–thaw cycles, respectively). However, for the phantoms that underwent three freeze–thaw cycles, a significant difference in density measurements was observed between phantoms with glycerol concentrations of 0% and 20% ($p = 0.0374$), as well as between phantoms with 10% and 20% glycerol ($p = 0.003$). Despite these statistical differences, the absolute differences are less than 0.1 g/cm³.

The longitudinal sound speed measurements of the phantoms are provided in Figure 2B, and ranged from 1529 to 1660 m/s. For each glycerol concentration, the differences in longitudinal sound speed measurements between the numbers of freeze–thaw cycles were not

significant ($p = 0.22, 0.12$ and 0.31 for 0%, 10% and 15% glycerol, respectively), except for those of the phantoms with 20% glycerol concentration, which underwent two and three freeze–thaw cycles ($p = 0.0498$). For each number of freeze–thaw cycles, the differences in the longitudinal sound speed measurements between the phantoms of varying glycerol concentrations were significant ($p < 0.001$ for the phantoms that underwent one, two and three freeze–thaw cycles). The longitudinal sound speed increased significantly with increasing glycerol concentration. A linear regression of sound speed measurements as a function of glycerol concentration was performed for each number of freeze–thaw cycles. The resulting linear functions of longitudinal sound speed (c_{li}) for the i th freeze–thaw cycle are given as $c_{1i} = (1527 + 6.31x)$ m/s, $c_{12} = (1534 + 6.29x)$ m/s and $c_{13} = (1541 + 5.77x)$ m/s, respectively, where x denotes the glycerol concentration (% v/v). The goodness-of-fit R^2 for the phantoms that underwent one, two and three freeze–thaw cycles is 0.96, 0.97 and 0.94, respectively.

The frequency-dependent acoustic attenuation and power-law fit coefficients are provided in Figure 3. For all phantom types, attenuation increases non-linearly with increasing frequency (Fig. 3A–C). The R^2 values of the power-law fit equations to the attenuation data for all phantom types are greater than 0.84. The power fit constants (α_0) and exponents (n) are given in Figure 3D and 3E, and ranged from 0.02 to 0.1 dB/cm/MHz ^{n} and 1.6 to 1.9, respectively.

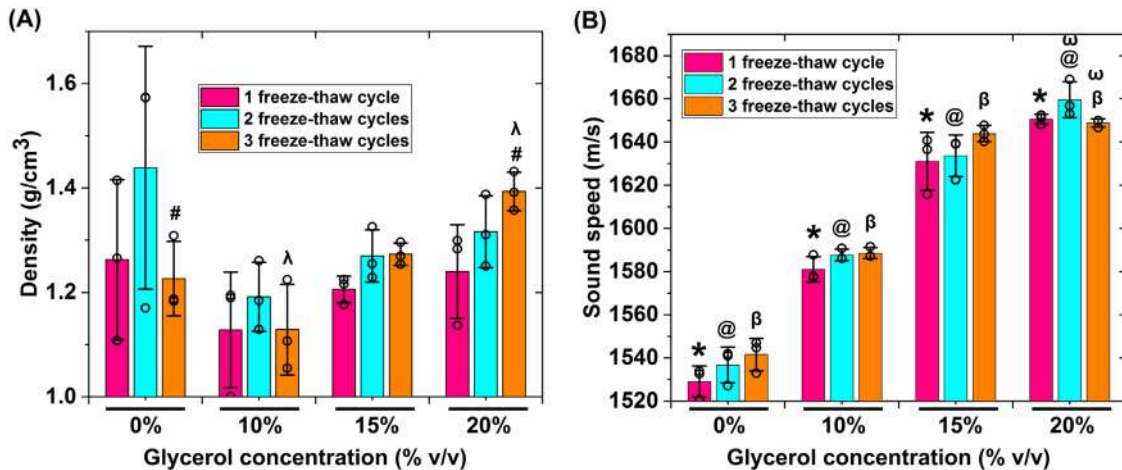


Fig. 2. Measured (A) densities and (B) longitudinal sound speeds of the phantoms. Means \pm standard deviations of three samples per phantom type are shown. Individual data points are presented as *hollow circles*. A one-way analysis of variance with Tukey's *post hoc* test was performed to compare data. The hash symbol (#) and lambda (λ) represent $p < 0.05$ for comparing the density measurements between phantoms that underwent three freeze–thaw cycles with glycerol concentrations of 0% and 20%. Lambda (λ) represents $p < 0.05$ for comparing the density measurements between phantoms that underwent three freeze–thaw cycles with glycerol concentrations of 10% and 20%. Omega (ω) represents significantly different sound speed measurements between phantoms with 20% glycerol concentration that underwent two and three freeze–thaw cycles. The *, @ and β represent $p < 0.05$ for the sound speed measurements between glycerol concentrations for phantoms that underwent one, two and three freeze–thaw cycles, respectively.

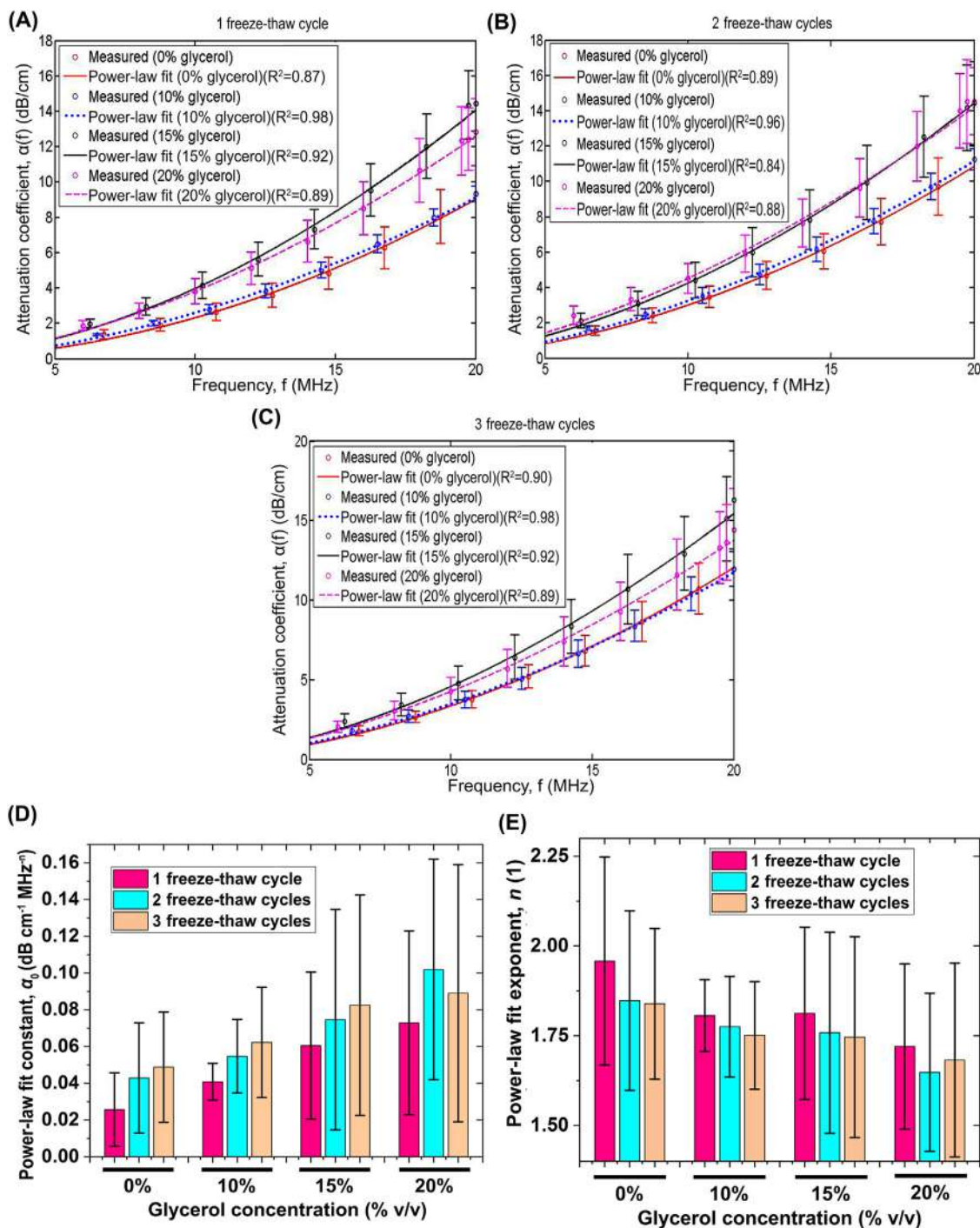


Fig. 3. Frequency-dependent attenuation spectra of polyvinyl alcohol phantoms with different glycerol concentrations that underwent (A) one, (B) two and (C) three freeze-thaw cycles. Means \pm standard deviations of three samples per phantom type are shown. (D) Power-law fit constant α_0 and (E) power-law fit exponent n of the frequency-dependent attenuation of the phantoms. Mean and 95% confidence bounds are shown.

Note that each error bar represents the 95% confidence interval of a regression coefficient, that is, the power fit constant (Fig. 3D) or the fit exponent (Fig. 3E). The observed variability in the power-law fit constants and

exponents may be due to experimental measurement errors, inhomogeneities in the scatterer spatial distributions caused by particle clumping or inhomogeneities in the phantom material.

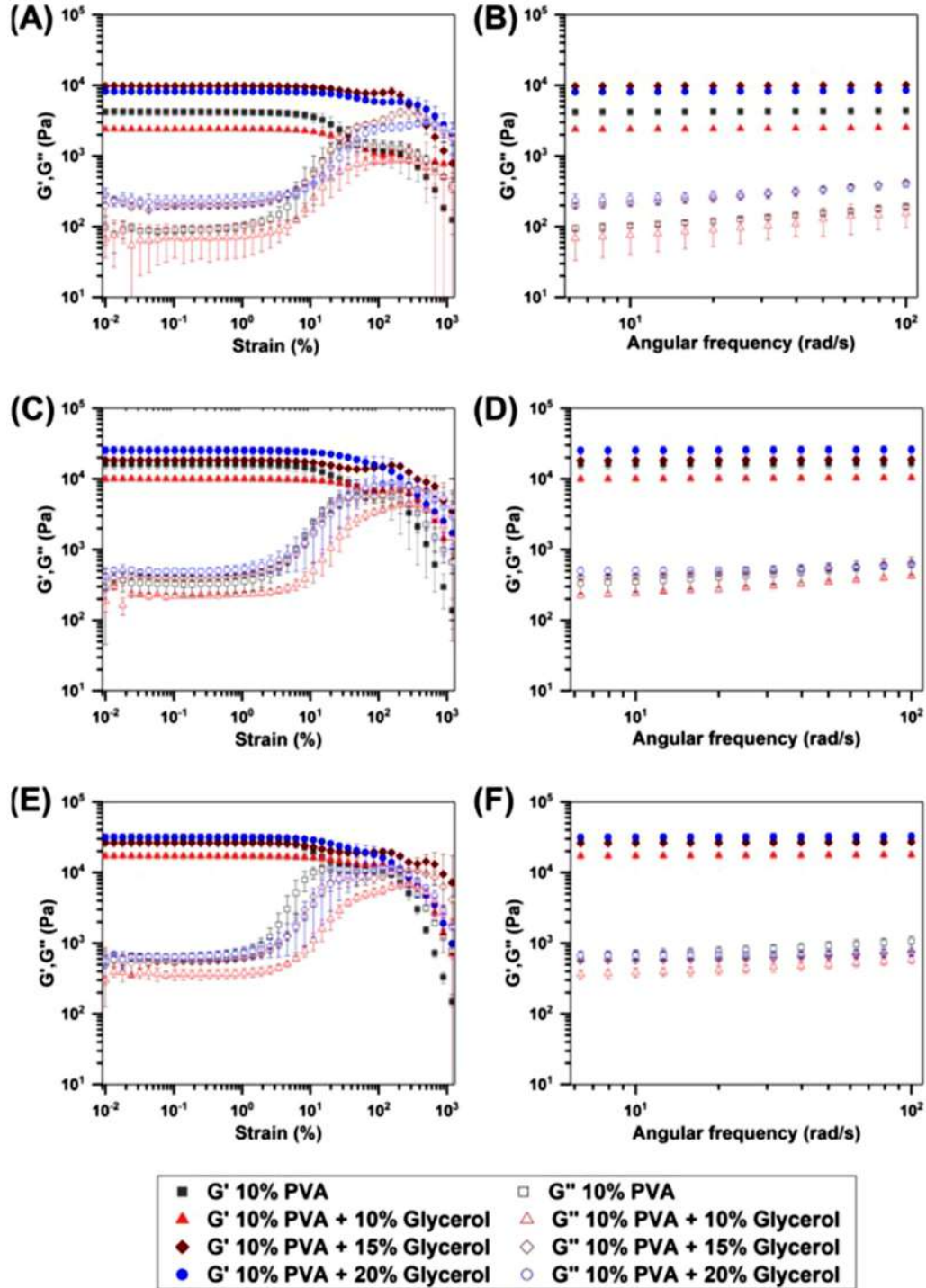


Fig. 4. Amplitude scan measurements of phantoms that underwent (A) one freeze–thaw cycle, (C) two freeze–thaw cycles and (E) three freeze–thaw cycles. Frequency scan measurements of phantoms that underwent (B) one freeze–thaw cycle, (D) two freeze–thaw cycles and (F) three freeze–thaw cycles. G' and G'' correspond to the storage modulus and loss modulus, respectively. Means \pm standard deviations of three samples per phantom type are shown.

Viscoelasticity measurements using rheometry

The amplitude sweep tests of phantoms are illustrated in Figure 4A, 4C, and 4E. Amplitude scan plots help indicate the limit of the LVR (0.01%–1% strain (γ))

range). Beyond this limit, both G' and G'' varied as a function of γ because of the microstructural changes in the phantoms. However, there was no visible change in the appearance of the phantoms. Hence, subsequent

frequency scan measurements were performed at 0.5% γ within the LVR. The frequency scans of the phantoms are provided in Figure 4B, 4D and 4F and range from 1 to 16 Hz (angular frequencies of 6.3 to 100 rad/s). G' and G'' decreased with 10% glycerol and increased with 15% and 20% glycerol, irrespective of the number of freeze–thaw cycles.

Viscoelasticity estimates using the KV model

The shear modulus estimates of the phantoms are illustrated in Figure 5A and range from 2.39 to 36.1 kPa. For each glycerol concentration, the shear modulus estimates increased with increasing number of freeze–thaw cycles. For each number of freeze–thaw cycles, the shear moduli of PVA phantoms with 10% (v/v) glycerol did not significantly differ from those of phantoms without glycerol at 0% glycerol concentration ($p = 0.10$, 0.13 and 0.10 for the phantoms that underwent one, two and three freeze–thaw cycles, respectively). Correlation analysis revealed a significant and moderate positive correlation ($r = 0.73$, $p = 0.02$) between shear modulus estimates and glycerol concentrations ranging from 10% to 20% (v/v) for phantoms that underwent one freeze–thaw cycle. For the phantoms that underwent two and three freeze–thaw cycles, a significant and strong positive

correlation between shear modulus estimates and glycerol concentrations from 10% to 20% (v/v) was observed ($r = 0.97$, $p = 0.000025$, for two freeze–thaw cycles, and $r = 0.95$, $p = 0.0012$, for three freeze–thaw cycles).

For estimating viscosity, a linear regression was performed on the frequency-dependent loss modulus measurements. The R^2 values of the KV model fits ranged from 0.63 to 0.85. In Figure 5B, representative loss modulus measurements and the KV model fit are shown for a PVA phantom with 15% (v/v) glycerol, which underwent two freeze–thaw cycles. The viscosity estimates, illustrated in Figure 5C, varied in the range 1.63 to 17.7 Pa·s. For each glycerol concentration, the viscosity estimates increased with increasing number of freeze–thaw cycles. For the phantoms that underwent one and two freeze–thaw cycles, the viscosity estimates of the phantoms with 10% (v/v) glycerol were not significantly different from those without glycerol at 0% concentration ($p = 0.36$ for one freeze–thaw cycle, and $p = 0.1$ for two freeze–thaw cycles). However, for the phantoms that underwent three freeze–thaw cycles, these differences were significant ($p = 0.0099$). Furthermore, for each number of freeze–thaw cycles, an increasing trend in viscosity estimates was observed for phantoms with increasing glycerol concentrations from

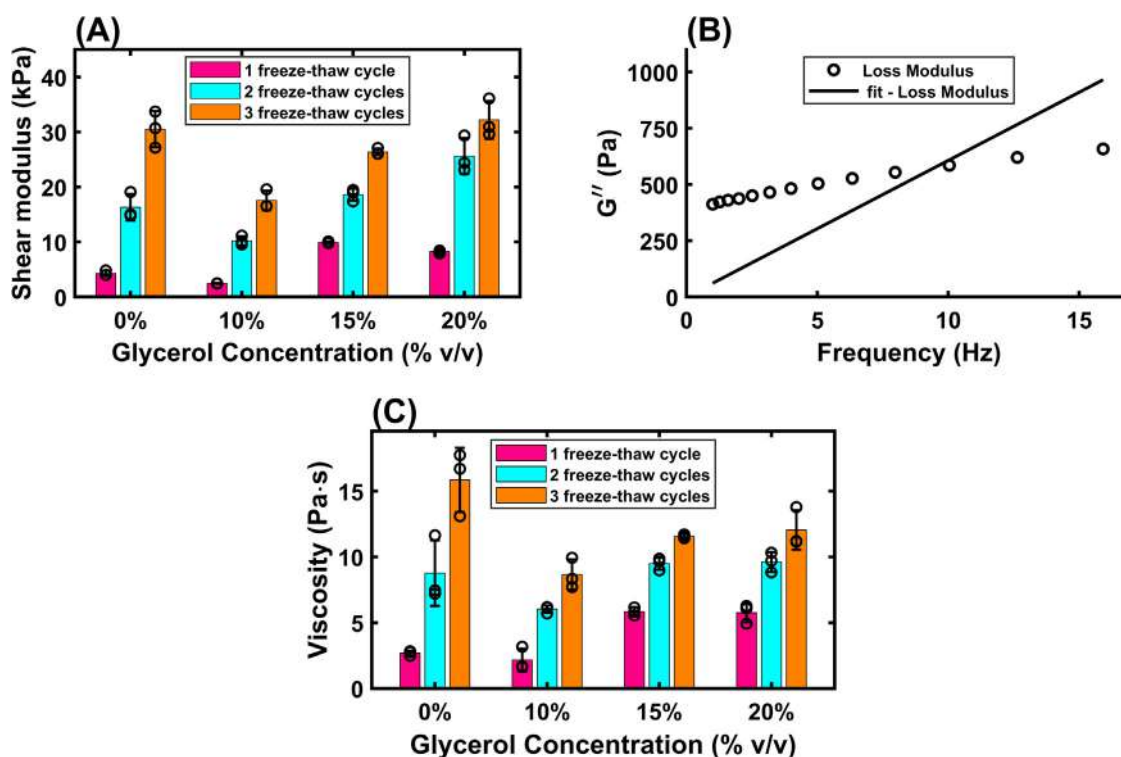


Fig. 5. (A) Shear modulus estimates of phantoms assuming a Kelvin–Voigt model. (B) Representative loss modulus G'' measurements with the Kelvin–Voigt model curve fit for a phantom with 15% (v/v) glycerol that underwent two freeze–thaw cycles. (C) Viscosity estimates of the phantoms. Means \pm standard deviations of three samples per phantom type are shown. Individual data points are presented as hollow circles.

10% to 20% (v/v). Specifically, correlation analysis revealed a significant and moderate to strong positive correlation between viscosity estimates and glycerol concentrations ranging from 10% to 20% (v/v) for phantoms that underwent one and two freeze–thaw cycles ($r = 0.81$, $p = 0.007$, and $r = 0.73$, $p = 0.03$, respectively). For the phantoms that underwent three freeze–thaw cycles, no significant correlation ($r = 0.63$, $p = 0.08$) between viscosity measurements and glycerol concentrations from 10% to 20% v/v was observed.

Viscoelasticity estimates using the KVFD model

The frequency-dependent shear wave speed estimates were computed according to eqn (5), and a least squares non-linear regression was performed to obtain the KVFD parameters of the phantoms. In Figure 6A, representative estimates of shear wave speed, c_s , and the KVFD model fit are shown for a PVA phantom with 15% (v/v) glycerol that underwent two freeze–thaw cycles. The R^2 values for KVFD fitting for all phantom types ranged from 0.93 to 0.99.

The μ_0 parameter estimates of the phantoms, illustrated in Figure 6B, range from 0.68 to 15.0 kPa. For each glycerol concentration, the μ_0 estimates increased with increasing number of freeze–thaw cycles. For one

freeze–thaw cycle, the μ_0 estimates of PVA phantoms with 10% (v/v) glycerol were not significantly different than those of phantoms without glycerol at 0% concentration ($p = 0.10$). However, these differences were significant for the phantoms that underwent two and three freeze–thaw cycles ($p = 0.008$ and $p = 0.0018$, respectively). Correlation analysis revealed no significant correlation between μ_0 measurements and glycerol concentrations ranging from 10% to 20% (v/v) for phantoms that underwent one freeze–thaw cycle ($r = 0.66$, $p = 0.055$). However, for the phantoms that underwent two and three freeze–thaw cycles, a significant and strong positive correlation ($r = 0.97$, $p = 0.000025$, for two freeze–thaw cycles, and $r = 0.95$, $p = 0.000079$, for three freeze–thaw cycles) was observed between μ_0 estimates and glycerol concentrations from 10% to 20% (v/v).

The μ_a estimates, illustrated in Figure 6C, varied in the range $1.36(\text{kPa} \cdot \text{s})^a$ to $19.8(\text{kPa} \cdot \text{s})^a$. For each glycerol concentration, the μ_a estimates increased with increasing number of freeze–thaw cycles. For the phantoms that underwent one freeze–thaw cycle, the μ_a estimates of the phantoms with 10% glycerol were not significantly different from those without glycerol at 0% concentration ($p = 0.10$). However, these differences were significant for the phantoms that underwent two and three

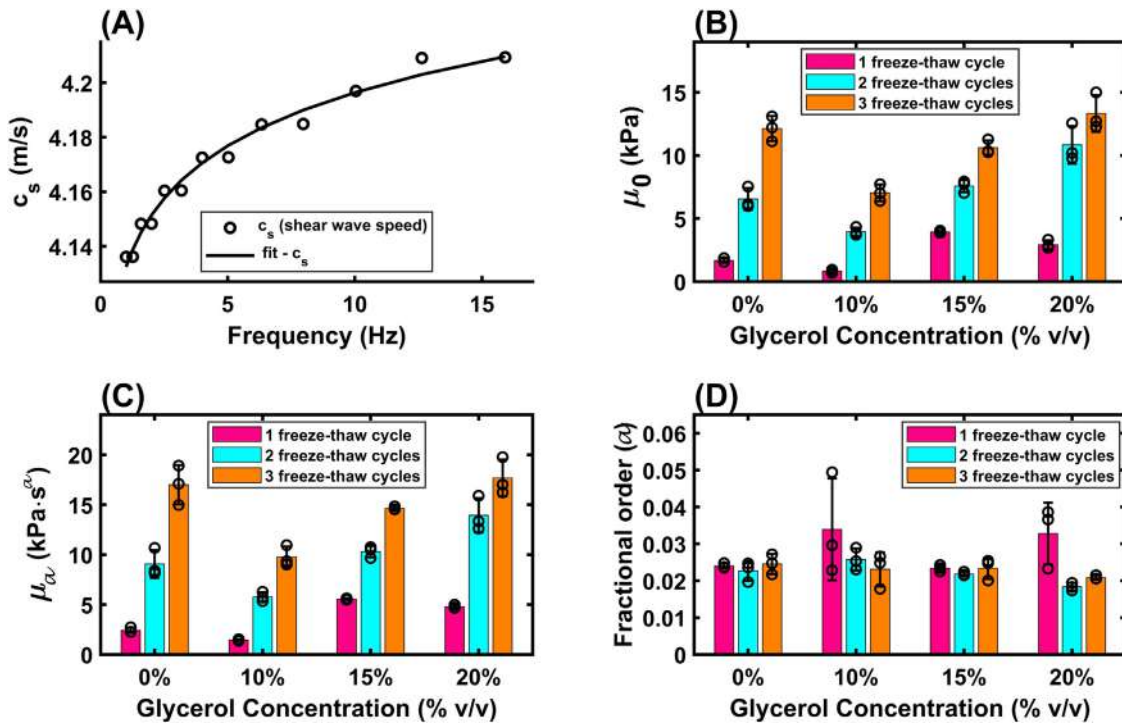


Fig. 6. (A) Representative frequency-dependent shear wave speed (c_s) estimates, assuming a Kelvin–Voigt fractional derivative (KVFD) model, and least squares non-linear curve fit for a phantom with 15% (v/v) glycerol that underwent two freeze–thaw cycles and was assessed by rheometry. Three-parameter estimates of the KVFD model fits: (B) μ_0 , (C) μ_a and (D) fractional order α . Means \pm standard deviations of three samples per phantom type are shown. Individual data points are presented as *hollow circles*.

freeze–thaw cycles ($p = 0.018$ and $p = 0.0050$, respectively). Furthermore, for each number of freeze–thaw cycles, an increasing trend in μ_a estimates was observed for phantoms with increasing glycerol concentrations from 10% to 20% (v/v). Correlation analysis revealed a significant and moderate positive correlation between μ_a estimates and glycerol concentrations ranging from 10% to 20% (v/v) ($r = 0.76$, $p = 0.016$) for phantoms that underwent one freeze–thaw cycle. For the phantoms that underwent two and three freeze–thaw cycles, a significant and strong positive correlation between μ_a estimates and glycerol concentrations from 10% to 20% (v/v) was observed ($r = 0.96$, $p = 0.000026$, and $r = 0.94$, $p = 0.00011$, respectively). The fractional order parameter a was in the range 0.017 to 0.049, as illustrated in Figure 6D.

Comparisons of phantom microstructure and viscoelasticity measurements

Field emission scanning electron microscopy of the phantoms revealed the effect of microstructural changes on the viscoelasticity measurements of phantoms with varying concentrations of glycerol (Fig. 7). A porous

hydrogel network without glycerol and a non-porous structure with glycerol are seen in FE-SEM images, irrespective of their glycerol concentrations. The phantoms without glycerol exhibited an increase in pore size as the number of freeze–thaw cycles increased. Image analysis revealed an average of 45% porosity for the phantoms that underwent one freeze–thaw cycle, 56% porosity for the phantoms that underwent two freeze–thaw cycles and 62% that porosity for the phantoms underwent three freeze–thaw cycles.

DISCUSSION

The present study was aimed at developing viscoelastic PVA phantoms for applications in ultrasound elastography. PVA phantoms with varying glycerol concentrations (0%, 10%, 15% and 20% v/v) were fabricated and subjected to one, two or three freeze–thaw cycles. The density of phantoms was estimated using the water displacement method. The longitudinal sound speed and attenuation measurements were performed using the through-transmission substitution method.

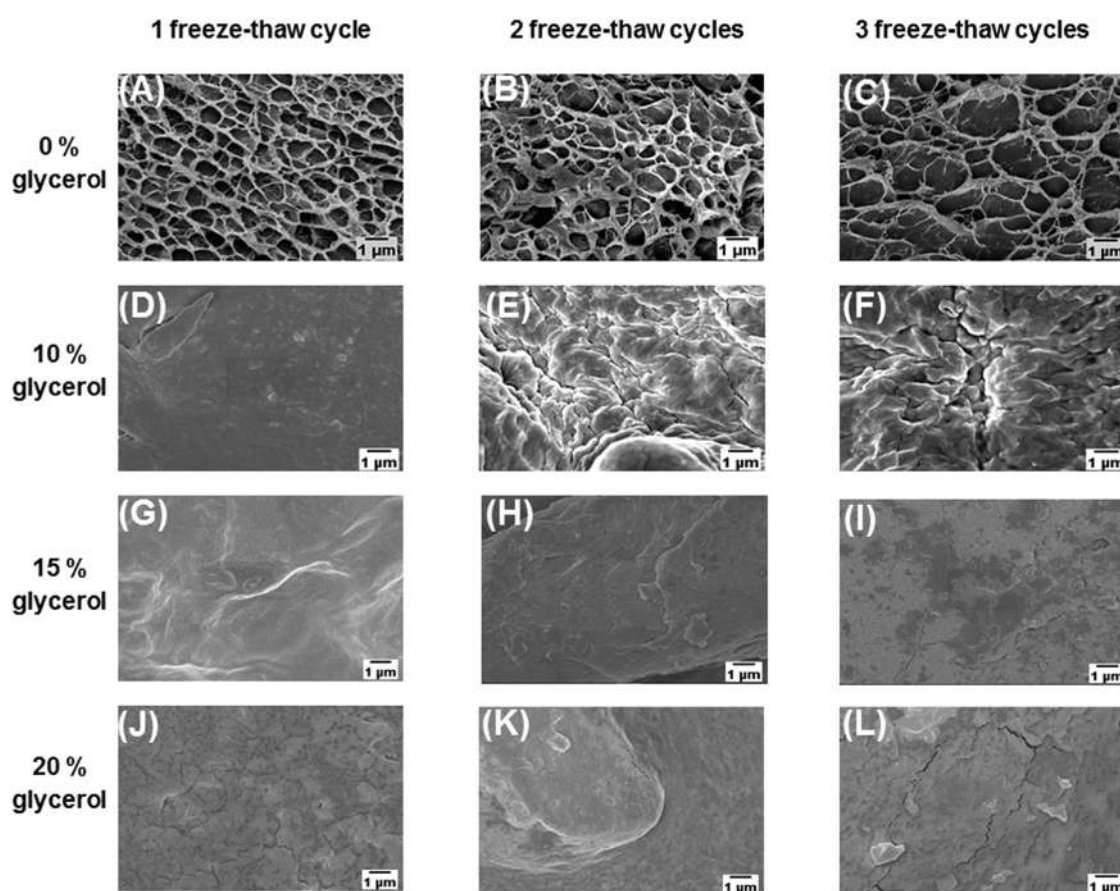


Fig. 7. Representative scanning electron microscopy images of the polyvinyl alcohol phantoms with various concentrations of glycerol and numbers of freeze–thaw cycles. Bar = 1 μm .

Viscoelastic measurements were obtained using a rheometer. To investigate the relationship between phantom structure and viscoelasticity measurements, the surface morphology and microstructure of the phantoms with varying glycerol concentrations were observed through scanning electron microscopy.

Density, longitudinal sound speed and attenuation measurements

The density and longitudinal sound speed measurements of the PVA phantoms were within the range of densities of soft tissues, such as liver, muscle, brain, fat, kidney and breast tissue (Culjat *et al.* 2010; Ambrogio *et al.* 2020; McGarry *et al.* 2020). Both density and longitudinal sound speed measurements were also similar to those previously published for PVA-based phantoms, as outlined in Table 1 (Courmane *et al.* 2010; Mercado-Shekhar *et al.* 2018; Ambrogio *et al.* 2020; Galvis-García *et al.* 2020; Villa *et al.* 2020). In the present study, the addition of glycerol in PVA phantoms increased their longitudinal sound speeds (Fig. 2B). Because the longitudinal sound speed in glycerol (1964 m/s) (Fergusson *et al.* 1954) is greater than that in water (1497 m/s) (Greenspan and Tschiegg 1957) at room temperature, increasing the concentration of glycerol in the hydrogel phantom caused an increase in the longitudinal sound speed. Similar observations were seen by Cabrelli *et al.* (2017), who reported that increasing the concentration of glycerol in an oil-based phantom increased the longitudinal sound speed from 1423 to 1502 m/s. In another study, Courmane *et al.* (2010) also observed that as the glycerol concentration in PVA-based phantoms increased from 8% to 16% by weight, the longitudinal sound speed increased from 1542 to 1587 m/s.

In the present study, increasing the number of freeze–thaw cycles generally did not affect the longitudinal sound speed significantly, although there was a significant difference in longitudinal sound speed measurements between the phantoms with 20% glycerol

concentration that underwent two and three freeze–thaw cycles. However, this difference was only approximately 10 m/s. All measured sound speeds were within the range of soft tissues, such as human gallbladder (1583 m/s), liver tissue (1592 m/s), cervix (1633 m/s) and dermis (1645 m/s) (Sehgal *et al.* 1986; Duck 1990; Chen *et al.* 2016).

The measured frequency-dependent acoustic attenuation of all phantoms followed a power-law relationship. These estimates are within the range of previously reported attenuation coefficients ranging from 0.01 to 1.03 dB/cm/MHzⁿ with power-law exponents of 1–2.04 of soft tissues and other PVA-based phantoms (Table 1) (Duck 1990; Chen *et al.* 2016; Ambrogio *et al.* 2020).

Viscoelasticity estimates

Notably, PVA phantoms exhibited an increase in viscosity with the number of freeze–thaw cycles, even without the use of glycerol as an additive. Rheometer data analyzed assuming the KV model revealed increasing trends in both shear modulus and viscosity values with increasing freeze–thaw cycles (Fig. 5). Similarly, rheometer data analyzed assuming the KVFD model revealed increasing trends in μ_0 and μ_a with increasing number of freeze–thaw cycles. These observations indicate that increasing the number of freeze–thaw cycles affects both the elastic and viscous properties of PVA phantoms. In elastography literature, it has been noted that increasing the number of freeze–thaw cycles results in an increase in the shear modulus of PVA phantoms. However, the effect of the number of freeze–thaw cycles on viscosity has not been explored previously. Here, our findings indicate that the viscosity of the PVA phantom is also significantly affected in this process, which can cause significant errors in ultrasound elastography measurements conducted using linear elastic assumptions.

Table 1. Acoustic properties of PVA-based tissue-mimicking phantoms from the present study and published literature

Phantom description	Density (g/cm ³)	Longitudinal speed of sound (m/s)	Acoustic attenuation power fit coefficients	
			α (dB/cm/MHz ⁿ)	n
PVA with 0, 10%, 15% and 20% glycerol (present study)	1.12–1.44	1529–1660	0.02–0.10 @ 5–20 MHz	1.6–1.9 @ 5–20 MHz
PVA (Mercado-Shekhar <i>et al.</i> 2018)	1.064	1535	—	—
PVA with varying sucrose concentrations (Villa <i>et al.</i> 2020)	1.05–1.33	1536–1819	—	—
PVA with thermochromic material (Ambrogio <i>et al.</i> 2020)	—	1562	0.13 @ 1–20 MHz	1.5 @ 1–20 MHz
PVA with 8%, 12% and 16% glycerol (Courmane <i>et al.</i> 2010)	—	1542–1587	—	—

PVA = polyvinyl alcohol.

Table 2. Viscoelastic properties of tissue-mimicking phantoms and tissues measured by rheometry and assuming a Kelvin–Voigt model

Tissue-mimicking phantom/tissue	Oscillation frequency sweep range (Hz)	Shear modulus (kPa)	Shear viscosity (Pa·s)
PVA with 0, 10, 15 and 20% (v/v) glycerol (present study)	1–16	2.39–36.1	1.63–17.7
PVA (Guo et al. 2019)	1–20	1.34	9.67
Oil-in-gelatin phantoms (Zhu et al. 2015)	1–40	1.06–4.29	2.52–4.90
Rat liver normal and different fibrosis stages (Zhu et al. 2016)	1–40	0.62–1.70	3.38–4.63

PVA = polyvinyl alcohol.

Prior to the present study, viscoelasticity measurements of PVA phantoms made with glycerol using direct mechanical testing methods have not been reported. In Table 2, the viscoelasticity measurements of tissue-mimicking phantoms and tissues from prior studies are presented along with the results from the current study. Note that the studies reported in Table 2 performed rheometer measurements and estimated the shear modulus and viscosity parameters using the KV model. Other studies have investigated the viscoelastic nature of tissue-mimicking phantoms and soft tissues using ultrasound elastography and direct mechanical tests (Narita et al. 2013; Sjöstrand et al. 2020). However, the differences in the techniques have made it challenging to directly compare the exact values of the viscoelastic measurements. Nonetheless, Table 2 provides insights into how the measurements of our present studies compare with those of prior literature using the KV model.

Recently, Guo et al. (2019) reported that phantoms composed of 10% PVA had an average shear modulus of 1.34 kPa and viscosity of 9.67 Pa·s. They conducted rheometry of the phantoms at 1–20 Hz and fitted a KV model to the complex shear modulus, to extract shear modulus and viscosity parameters (Guo et al. 2019). In the present study, the values of the measured shear modulus and viscosity of PVA phantoms without glycerol are close to the values mentioned by Guo et al. (Table 2). Additionally, we determined the feasibility of obtaining a wide range of viscoelasticity values using our approach.

In comparison to another type of phantom, Zhu et al. (2015) investigated the viscoelastic properties of oil-in-gelatin phantoms using a rotary rheometer at 1–40 Hz, assuming the KV model. Their elasticity measurements increased when the castor oil concentration increased from 0% to 20%, but decreased for 30% and 40% oil concentrations (Zhu et al. 2015). However, their viscosity measurements consistently increased from a mean of 2.5 to 4.9 Pa·s as the castor oil concentration increased from 0% to 40%. Their viscosity measurements of oil-in-gelatin phantoms are within the range of those of the PVA phantoms without and with 10% glycerol in the current study (Table 2).

The shear modulus and viscosity estimates reported in the present study and based on the KV model are consistent with those of a variety of healthy and diseased soft tissues. Zhu et al. (2016) studied different stages of liver fibrosis, F0 to F4, in rat livers and measured the corresponding viscoelastic properties through rheological experiments conducted at 1–40 Hz. The authors reported that the shear modulus and viscosity of fibrotic liver using the KV model are higher than those of normal liver. The reported values of shear modulus and viscosity for the fibrotic liver are on average 1.616 kPa (F3)/1.644 kPa (F4) and 4.443 Pa·s (F3)/4.060 Pa·s (F4), respectively, whereas for normal liver the values are on average 0.618 kPa and 3.379 Pa·s, respectively. These values are similar to the shear modulus and viscosity obtained in this study for phantoms with 0% and 10% glycerol that underwent one freeze–thaw cycle. Therefore, the phantoms developed in the present study can mimic different stages of liver fibrosis and help validate ultrasound elastography approaches (Zhu et al. 2016).

The trends in the shear modulus estimates using the KV model (Fig. 5A) and the μ_0 estimates using the KVFD model (Fig. 6B) are similar. Furthermore, the μ_0 estimates using the KVFD model of the PVA phantoms with and without 10% glycerol, subjected to one freeze–thaw cycle, are within the range of values reported for gelatin phantoms (*i.e.*, 2.61–9.92 kPa) by Gomez et al. (2022). However, the viscosity-related parameter and fractional order of the PVA phantoms in the current study are different from those of these gelatin phantoms, possibly because of the differences in the materials used (Gomez et al. 2022). In the present study, the trends in the viscosity estimates using the KV model were comparable to those of the viscosity-related parameter μ_a using the KVFD model. Specifically, the viscosity of the PVA phantoms increased as the glycerol concentration increased from 10% to 20% (v/v). The fractional order a values for the PVA phantoms (0.017–0.049) were within range of the a values obtained in a previous study that investigated the viscoelastic properties of oil-in-gelatin phantoms (0.045–0.049) (Poul and Parker 2022). In the current study, the R^2 values of the KVFD model

curve fits to the rheometry data ($R^2 = 0.93\text{--}0.99$) were higher than those of the KV model fits ($R^2 = 0.63\text{--}0.85$).

At low glycerol concentrations (0 and 10% v/v), the shear modulus and viscosity-related parameters of the PVA phantoms decreased, as illustrated in [Figures 5 and 6](#), whereas, at higher glycerol concentrations (15% and 20% v/v), the shear modulus and viscosity-related parameters of the PVA gels increased. Previously reported studies may provide some insight into this observation. [Mohsin et al. \(2011\)](#) studied the effect on thermal and mechanical properties of cryogels with 5% PVA and relatively-low concentrations of glycerol (0.5%, 1% and 2%). The mechanical properties of the gels were measured by nano-indentation. They revealed that glycerol served as a plasticizer because of its low molecular weight and the presence of hydroxyl groups. The embedment of small molecules of glycerol between the PVA polymer chains, which promotes polymer–plasticizer interactions and weakens polymer–polymer interactions, leads to an increase in the free volume and spacing and makes the polymeric network less dense. As a result, the elastic modulus decreased ([Mohsin et al. 2011](#)). These results are in accordance with the observations from the present study, wherein the shear modulus of phantoms with 10% glycerol was less than that of the phantom without glycerol.

In contrast, [Cournane et al. \(2010\)](#) observed that increasing glycerol concentration from 8% to 16% by weight led to an increase in the Young's modulus of cryogels with 5–6 wt% PVA, as measured by compression testing. In the current study, a similar increase in the shear modulus was observed for 15% and 20% glycerol phantoms relative to those with 10% glycerol. [Cournane et al. \(2010\)](#) noted that the addition of glycerol affected the cross-linking and gelation of the PVA phantoms. To initiate the cross-linking process for PVA, the desired minimum freezing temperature is -20°C . Increasing the concentration of glycerol reduces the freezing temperature of the PVA solution, making the sample rigid. Additionally, as glycerol is a viscous fluid, increasing its concentration increases the viscosity of PVA phantoms.

Comparisons of phantom microstructure and viscoelasticity measurements

[Holloway et al. \(2013\)](#) reported that the porosity of PVA hydrogels (determined using optical microscopy) increased with the increase in the number of freeze–thaw cycles. There are two potential reasons for this observation. First, as water in the gels freezes, microstructural remodeling of PVA occurs. The water is expelled from the PVA matrix, creating concentrated regions of the polymer ([Wan et al. 2014](#)). Second, the water freezes and expands with each cycle, which pushes the PVA chains close to each other, reducing the distance between them, which facilitates

hydrogen bonding, crystallite formation and increased gel porosity ([Wan et al. 2014](#)). In a related study by [Wang et al. \(2016\)](#), chitosan hydrogels with hydroxypropyl methylcellulose (HPMC) alone exhibited a porous network, while chitosan gels with HPMC and glycerol did not exhibit a porous structure. [Wang et al. \(2016\)](#) noted that the addition of glycerol destroyed the homogeneous structure of the hydrogels and that glycerol played a dual role as a water-retaining agent to chitosan and as a dehydrator to HPMC. Similar to the case of chitosan, glycerol forms extensive hydrogen bonds with PVA ([Mohsin et al. 2011](#)).

In the present study, the effect of microstructural differences on the viscoelasticity of the phantoms with various glycerol concentrations could not be ascertained because all the SEM images of phantoms with glycerol revealed a non-porous structure, irrespective of their glycerol concentrations ([Fig. 7](#)). Therefore, SEM analysis was inadequate for understanding the relationship between viscoelasticity and the microstructure of the phantoms. Because SEM only enables visualization of the surface morphology of phantoms, the microstructure of the inner regions of the phantoms could not be assessed without cutting the phantom. Future work will involve further investigations on identifying the cause of differences in the viscoelasticity of phantoms with varying concentrations of glycerol.

Study limitations

In this study, rheometry measurements were performed for frequencies ranging from 1 to 16 Hz. However, frequencies for clinical dynamic elastography methods, such as transient elastography and shear wave elastography, may range from 50 to 1000 Hz. Therefore, values from the rheometer measurements may not exactly match the dynamic elastography results, which is a limitation of this work. In previous study, [Zhu et al. \(2015\)](#) reported differences in measurement values between rheometry and dynamic elastography measurements (*i.e.*, shear wave ultrasound dispersion vibrometry [SDUV] and acoustic radiation force imaging [ARFI]), which may be attributed to the differences in the frequency ranges. [Gomez et al. \(2022\)](#) fitted the KVFD model on a shear dispersion curve, which included a combination of measurements by rheometry for low shear frequencies (0.5–4.5 Hz) and a shear wave tracking optical method (using a high-speed camera) for the higher frequencies (>50 Hz) to estimate the viscoelastic properties of their gelatin phantoms. In the present study, the KVFD model was fitted to the rheometry data over the range 1–16 Hz, which is a limitation of our work. In subsequent studies, we plan to use a combination of rheometry and shear wave imaging to estimate viscoelastic parameters over a wider shear wave frequency range, including the range relevant for ultrasound elastography.

Contributions of the work

The principal contributions of this work are (i) the development and characterization of viscoelastic PVA phantoms created by the addition of glycerol, and (ii) the finding that the viscosity of PVA phantoms increases with the number of freeze–thaw cycles, even in the absence of glycerol. The first contribution allows researchers to create phantoms in the lab for testing dynamic viscoelasticity imaging (*i.e.*, viscoelastography) methods, such as shear wave elastography. The second contribution is important because it underscores shear wave elastography measurements of PVA phantoms, which are based on linear elastic assumptions and may be confounded by changes the viscosity of PVA created by multiple freeze–thaw cycles.

Other than ultrasound elastography, PVA phantoms have been investigated as potential ultrasound therapy phantoms (Ambrogio *et al.* 2020; Braunstein *et al.* 2022). The viscoelastic properties of these phantoms could potentially have an impact on therapeutic ultrasound applications, especially those based on cavitation effects. Further studies can be conducted to determine these effects.

CONCLUSIONS

In this study, PVA phantoms with and without glycerol additives were characterized for applications in ultrasound elastography. The density, speed of sound, acoustic attenuation and viscoelastic parameters using two models, that is, the Kelvin–Voigt and Kelvin–Voigt fractional derivative models, were estimated. The addition of glycerol was found to modify the viscoelastic properties of the PVA phantoms. The shear modulus and viscosity of the PVA phantoms were found to decrease with 10% glycerol and increase with 15% and 20% glycerol. Notably, the viscosity of PVA phantoms increased with the number of freeze–thaw cycles, even in the absence of glycerol. The general trends were consistent for both KV and KVFD models. These results are important to consider because it could affect shear wave elastography measurements of PVA phantoms, which are based on linear elastic assumptions. SEM analysis revealed microstructural changes in porosity induced in the hydrogels with the addition glycerol. The findings of this study could be useful for the laboratory validation of various ultrasound viscoelastography approaches.

Acknowledgments—K.P.M.-S. thanks the Gujarat State Biotechnology Mission (GSBTM), Government of Gujarat (Grant No. GSBTM/JD (R&D)/610/20-21/344) and the Indian Institute of Technology (IIT) Gandhinagar for financial support. P.T. acknowledges the Science and Engineering Research Board (Grant No. CRG/2020/006088) for funding. The authors acknowledge Professor Himanshu Shekhar, Professor Kevin Parker and Sedigheh Poul for useful discussions, as well as Jagruti Patil, Anushka Yadav, Boyapati Suresh, Devki Verma and Professor Superb Misra for their assistance in the preliminary stages of the work.

Conflict of interest disclosure—The authors declare they have no conflicts of interest.

Data availability statement—The data used in this study are available on request.

REFERENCES

- Amador C, Kinnick RR, Urban MW, Fatemi M, Greenleaf JF. Viscoelastic tissue mimicking phantom validation study with shear wave elasticity imaging and viscoelastic spectroscopy. *Proc IEEE Int Ultrason Symp* 2015;1–4.
- Ambrogio S, de Melo Baêso R, Gomis A, Rivens I, ter Haar G, Zeqiri B, Ramnarine KV, Fedele F, Miloro P. A polyvinyl alcohol-based thermochromic material for ultrasound therapy phantoms. *Ultrasound Med Biol* 2020;46:3135–3144.
- Asbach P, Klatt D, Hamhaber U, Braun J, Somasundaram R, Hamm B, Sack I. Assessment of liver viscoelasticity using multifrequency MR elastography. *Magn Reson Med* 2008;60:373–379.
- Braunstein L, Brüningk SC, Rivens I, Civalé J, ter Haar G. Characterization of acoustic, cavitation, and thermal properties of poly(vinyl alcohol) hydrogels for use as therapeutic ultrasound tissue mimics. *Ultrasound Med Biol* 2022;48:1095–1109.
- Cabrelli LC, Grillo FW, Sampaio DRT, Carneiro AAO, Pavan TZ. Acoustic and elastic properties of glycerol in oil-based gel phantoms. *Ultrasound Med Biol* 2017;43:2086–2094.
- Cao Y, Li GY, Zhang X, Liu YL. Tissue-mimicking materials for elastography phantoms: A review. *Extreme Mech Lett* 2017;17:62–70.
- Chen AI, Balter ML, Chen MI, Gross D, Maguire TJ, Yarmush ML. Multilayered tissue mimicking skin and vessel phantoms with tunable mechanical, optical, and acoustic properties. *Med Phys* 2016;43:3117–3131.
- Cournane S, Cannon L, Browne JE, Fagan AJ. Assessment of the accuracy of an ultrasound elastography liver scanning system using a PVA-cryogel phantom with optimal acoustic and mechanical properties. *Phys Med Biol* 2010;55:5965–5983.
- Cournane S, Fagan AJ, Browne JE. Review of ultrasound elastography quality control and training test phantoms. *Ultrasound* 2012;20:16–23.
- Culjat MO, Goldenberg D, Tewari P, Singh RS. A review of tissue substitutes for ultrasound imaging. *Ultrasound Med Biol* 2010;36:861–873.
- Duck FA. Acoustic properties of tissue at ultrasonic frequencies. In: *Physical properties of tissues: A comprehensive reference book*. San Diego, CA: Academic Press; 1990. p. 73–135.
- Ferguson FAA, Guptill EW, MacDonald AD. Velocity of sound in glycerol. *J Acoust Soc Am* 1954;26:67–69.
- Fromageau J, Brusseau E, Vray D, Gimenez G, Delachartre P. Characterization of PVA cryogel for intravascular ultrasound elasticity imaging. *IEEE Trans Ultrason Ferroelectr Freq Control* 2003;50:1318–1324.
- Funamoto K, Yamashita O, Hayase T. Poly(vinyl alcohol) gel ultrasound phantom with durability and visibility of internal flow. *J Med Ultrason* 2015;42:17–23.
- Galvis-García ES, Sobrino-Cossío S, Reding-Bernal A, Contreras-Marín Y, Solórzano-Acevedo K, González-Zavala P, Quispe-Siccha RM. Experimental model standardizing polyvinyl alcohol hydrogel to simulate endoscopic ultrasound and endoscopic ultrasound-elastography. *World J Gastroenterol* 2020;26:5169–5180.
- Gomez A, Callejas A, Rus G, Saffari N. Experimental evidence of shear waves in fractional viscoelastic rheological models. *Sci Rep* 2022;12:7448.
- Greenspan M, Tschiegg CE. Speed of sound in water by a direct method. *J Res Natl Bur Stand* 1957;59:249.
- Guo K, Zhu Y, Wang J, Jiang C, Yu J. Characterizing the viscoelastic properties of a tissue mimicking phantom for ultrasound elasticity imaging studies. *IOP Conf Ser Mater Sci Eng* 2019;490 022035.
- Hassan CM, Peppas NA. Structure and properties of poly(vinyl alcohol) (PVA). *Adv Polym Sci* 2000;153:37–65.
- Holloway JL, Lowman AM, Palmese GR. The role of crystallization and phase separation in the formation of physically cross-linked PVA hydrogels. *Soft Matter* 2013;9:826–833.
- Kumar K, Andrews ME, Jayashankar V, Mishra AK, Suresh S. Measurement of viscoelastic properties of polyacrylamide-based tissue-

- mimicking phantoms for ultrasound elastography applications. *IEEE Trans Instrum Meas* 2010;59:1224–1232.
- Manickam K, Machireddy RR, Seshadri S. Characterization of bio-mechanical properties of agar based tissue mimicking phantoms for ultrasound stiffness imaging techniques. *J Mech Behav Biomed Mater* 2014;35:132–143.
- McGarry CK, Grattan LJ, Ivory AM, Leek F, Liney GP, Liu Y, Miloro P, Rai R, Robinson A, Shih AJ, Zeqiri B, Clark CH. Tissue mimicking materials for imaging and therapy phantoms: A review. *Phys Med Biol* 2020;65:23TR01.
- Meral FC, Royston TJ, Magin R. Fractional calculus in viscoelasticity: An experimental study. *Commun Nonlinear Sci Numer Simul* 2010;15:939–945.
- Mercado-Shekar KP, Kleven RT, Aponte Rivera H, Lewis R, Karani KB, Vos HJ, Abruzzo TA, Haworth KJ, Holland CK. Effect of clot stiffness on recombinant tissue plasminogen activator lytic susceptibility in vitro. *Ultrasound Med Biol* 2018;44:2710–2727.
- Mohsin M, Hossin A, Haik Y. Thermal and mechanical properties of poly(vinyl alcohol) plasticized with glycerol. *J Appl Polym Sci* 2011;122:3102–3109.
- Nahirnyak VM, Yoon SW, Holland CK. Acousto-mechanical and thermal properties of clotted blood. *J Acoust Soc Am* 2006;119:3766–3772.
- Narita T, Mayumi K, Ducouret G, He P. Viscoelastic properties of poly(vinyl alcohol) hydrogels having permanent and transient cross-links studied by microrheology, classical rheometry, and dynamic light scattering. *Macromolecules* 2013;46:4174–4183.
- Nguyen MM, Zhou S, Robert JL, Shamdassani V, Xie H. Development of oil-in-gelatin phantoms for viscoelasticity measurement in ultrasound shear wave elastography. *Ultrasound Med Biol* 2014;40:168–176.
- Oglat AA, Matjafri MZ, Suardi N, Oglat MA, Abdelrahman MA, Oglat AA, Farhat OF, Alkhateb BN, Abdalrheem R, Ahmad MS, Abuazar MYM. Chemical items used for preparing tissue-mimicking material of wall-less flow phantom for Doppler ultrasound imaging. *J Med Ultrasound* 2018;26:123–127.
- Oudry J, Bastard C, Miette V, Willinger R, Sandrin L. Copolymer-in-oil phantom materials for elastography. *Ultrasound Med Biol* 2009;35:1185–1197.
- Parker KJ, Szabo T, Holm S. Towards a consensus on rheological models for elastography in soft tissues. *Phys Med Biol* 2019;64:215012.
- Poul SS, Parker KJ. Fat and fibrosis as confounding cofactors in viscoelastic measurements of the liver. *Phys Med Biol* 2022;66:045024.
- Poul SS, Ormachea J, Ge GR, Parker KJ. Comprehensive experimental assessments of rheological models' performance in elastography of soft tissues. *Acta Biomater* 2022;146:259–273.
- Raymond JL, Haworth KJ, Bader KB, Radhakrishnan K, Griffin JK, Huang SL, McPherson DD, Holland CK. Broadband attenuation measurements of phospholipid-shelled ultrasound contrast agents. *Ultrasound Med Biol* 2014;40:410–421.
- Sehgal CM, Brown GM, Bahn RC, Greenleaf JF. Measurement and use of acoustic nonlinearity and sound speed to estimate composition of excised livers. *Ultrasound Med Biol* 1986;12:865–874.
- Sjöstrand S, Meirza B, Grassi L, Svensson I, Camargo LC, Pavan TZ, Evertsson M. Tuning viscoelasticity with minor changes in speed of sound in an ultrasound phantom material. *Ultrasound Med Biol* 2020;46:2070–2078.
- Taghizadeh S, Labuda C, Mobley J. Development of tissue-mimicking phantom of the brain for ultrasonic studies. *J Acoust Soc Am* 2017;142:2564.
- Vieira SL, Pavan TZ, Junior JE, Carneiro AAO. Paraffin-gel tissue-mimicking material for ultrasound-guided needle biopsy phantom. *Ultrasound Med Biol* 2013;39:2477–2484.
- Villa E, Arteaga-Marrero N, González-Fernández J, Ruiz-Alzola J. Bimodal microwave and ultrasound phantoms for non-invasive clinical imaging. *Sci Rep* 2020;10:20401.
- Wan W, Bannerman AD, Yang L, Mak H. Poly(vinyl alcohol) cryogels for biomedical applications. In: Okay O, (ed). *Polymeric cryogels. Advances in Polymer Science*. Cham, Switzerland: Springer; 2014. p. 283–321. Vol. 263.
- Wang T, Chen L, Shen T, Wu D. Preparation and properties of a novel thermo-sensitive hydrogel based on chitosan/hydroxypropyl methylcellulose/glycerol. *Int J Biol Macromol* 2016;93:775–782.
- Zhou B, Zhang X. Comparison of five viscoelastic models for estimating viscoelastic parameters using ultrasound shear wave elastography. *J Mech Behav Biomed Mater* 2018;85:109–116.
- Zhu Y, Dong C, Yin Y, Chen X, Guo Y, Zheng Y, Shen Y, Wang T, Zhang X, Chen S. The role of viscosity estimation for oil-in-gelatin phantom in shear wave based ultrasound elastography. *Ultrasound Med Biol* 2015;41:601–609.
- Zhu Y, Chen X, Zhang X, Chen S, Shen Y, Song L. Modeling the mechanical properties of liver fibrosis in rats. *J Biomech* 2016;49:1461–1467.